A model of the guinea-pig ventricular cardiac myocyte incorporating a transverse-axial tubular system

Michal Pásek[a,b], Jiři Šimurda[b,c], Clive H. Orchard[d] and Georges Christé[e*]

[a] Institute of Thermomechanics, Czech Academy of Science - branch Brno, Czech Republic
[b] Department of Physiology, Faculty of Medicine, Masaryk University, Brno, Czech Republic
[c] Department of Biomedical Engineering, Faculty of Electrical Engineering and Communication, Brno, Czech Republic
[d] Department of Physiology, University of Bristol, Bristol BS8 1TD, United Kingdom
[e] INSERM, ADR Lyon, Lyon, France

Running title: Guinea-pig cardiac cell model with tubular system

Keywords: t-tubule; ion accumulation, ion depletion; extracellular space; TATS; restricted diffusion

Appendix 1 and Appendix 2 are provided as supplementary material.

* Corresponding author: Georges Christé

Present address:
Université Claude Bernard - Lyon 1,
Bâtiment Raphaël Dubois, 2° étage,
43 Bld du 11 Novembre 1918,
F-69622 Villeurbanne Cedex, France
Tel: (33)4 78 40 00 57 Fax: (33)4 72 44 79 37
Email: christe@lyon.inserm.fr

Abstract

A model of the guinea-pig cardiac ventricular myocyte has been developed that includes a representation of the transverse-axial tubular system (TATS), including heterogeneous distribution of ion flux pathways between the surface and tubular membranes. The model reproduces frequency-dependent changes of action potential shape and intracellular ion concentrations and can replicate experimental data showing ion diffusion between the tubular lumen and external solution in guinea-pig myocytes. The model is stable at rest and during activity and returns to rested state after perturbation. Theoretical analysis and model simulations show that, due to tight electrical coupling, tubular and surface membranes behave as a homogeneous whole during voltage and current clamp (maximum difference 0.9 mV at peak tubular I_{Na} of -38 nA). However during action potentials, restricted diffusion and ionic currents in TATS cause depletion of tubular Ca^{2+} and accumulation of tubular K^{+} (up to –19.8% and +3.4% respectively of bulk extracellular values, at 6 Hz). These changes, in turn, decrease ion fluxes across the TATS membrane and decrease sarcoplasmic reticulum (SR) Ca^{2+} load. Thus, the TATS plays a potentially important role in modulating the function of guinea-pig ventricular myocyte in physiological conditions.

Keywords: heart – ventricle – myocyte – model – guinea-pig

1. Introduction

The sarcolemma of cardiac ventricular myocytes has numerous invaginations which form a complex system of tubules (Pager, 1971; Page and McAllister, 1973; Forbes and Sperelakis, 1976), termed t-tubules or the transverse-axial tubular system (TATS: Forbes et al., 1984). However, unlike the t-tubular system of skeletal muscle cells (Huxley, 1964; Caillé et al., 1985), the physiological role of cardiac TATS is not fully understood.

Electrophysiologically, the capacitance current elicited by rectangular voltage-clamp pulses in cardiac ventricular myocytes shows a monoexponential decay, suggesting that the whole cell membrane is electrically well coupled. However there is increasing evidence that many ion flux pathways are located predominantly in the TATS membrane (see reviews by Scriven et al., 2000; Brette and Orchard, 2003), thereby endowing the TATS with specialised ion transfer properties.

The importance of changes of ion concentrations in the clefts between cardiac cells is well recognised (McGuigan, 1974; Attwell et al., 1979), but the possible consequences of accumulation and depletion of ions in cardiac TATS has only occasionally been considered (Bers, 1983; Bers and MacLeod, 1986; Yasui et al., 1993; Amsellem et al., 1994; Tourneur et al., 1994; Amsellem et al., 1995; Clark et al., 2001), although it has been suggested that restricted ion diffusion in cardiac TATS may produce significant changes of ion concentrations in its lumen (Bers, 1983; Yasui et al., 1993; Tourneur et al., 1994; Clark et al., 2001).

The complex interplay between changes in ion concentrations in the TATS lumen and the activity of ion channels, pumps and transporters present in the TATS membrane has been discussed (Christé, 1999; Brette and Orchard, 2003). However, until recently, there has been no attempt to determine quantitatively its physiological importance, despite the development of a number of computer models of ventricular cell electrophysiology and excitation-contraction (EC) coupling (see reviews by Noble, 2002 and Puglisi et al., 2004).

We have previously presented a model (Pasek et al., 2003) that incorporated TATS but combined features from several species such as guinea-pig, rat and dog. This model provided a general view of the physiological consequences of the TATS, but preliminary data indicated important species' differences in these consequences. Thus it was necessary to develop species-specific models that included TATS, in order to understand its role. The present work uses published data from the guinea-pig describing TATS morphology, ion pathway properties and distribution, intracellular Ca^{2+} handling and restricted ion diffusion between the TATS and

the extracellular space. We have chosen the guinea-pig ventricular myocyte because the distribution of several ion transfer mechanisms is known (Brette and Orchard, 2003), there already exist several mathematical models (Nordin, 1993; Nordin and Ming, 1995; Noble et al., 1998), there is a detailed quantitative description of its 3D morphology (Amsellem et al., 1994; Amsellem et al., 1995), its electrophysiology and Ca^{2+} handling are well characterised and it exhibits a "normal" action potential configuration. In the present study, the model is described, validated, and used to investigate: (i) the electrical properties of tubular and surface membranes; (ii) the effect of ion fluxes across the tubular membrane on ion concentrations within the TATS lumen; (iii) the reciprocal effect of these changes in lumenal ion concentrations on ion fluxes across the tubular membrane and consequently on intracellular ionic homeostasis.

2. Methods

We have used a biophysically realistic computer model of cardiac cell electrophysiology similar to those of Nordin (1993), Noble et al. (1998) and Faber and Rudy (2000). However, our model differs in two significant ways. First, new equations describing original experimental data from the guinea-pig were formulated and incorporated, where available. Secondly, a compartment representing the TATS, with restricted diffusion between the tubular and bulk extracellular space was included. The quantitative description of the ion transport systems in the tubular membrane is the same as that used for the surface membrane. The formulation of intracellular Ca^{2+} handling includes a restricted subsarcolemmal compartment (the dyadic space, referred to here as 'subspace'), network (NSR) and junctional (JSR) compartments of sarcoplasmic reticulum, and Ca^{2+} buffers. A schematic diagram of the model and an equivalent electrical circuit are shown in Fig. 1.

FIGURE 1 NEAR HERE

A) Schematic diagram of the ventricular cell model. B) Equivalent electrical circuit of the membrane systems.

A detailed formulation of the cell components and their integration into the complete model is described in the following sections and the complete set of model equations and parameters is given in the Appendix 1 provided as online supplementary material.

2.1. Geometric parameters of the cell and of the TATS

The dimensions of the guinea-pig ventricular myocyte have been reported by several groups (Amsellem et al., 1995; Wang et al., 1997; Shepherd and McDonough, 1998). On the basis of these data, the model cell is represented as a cylinder 130 μm in length and 12 μm in diameter. The volume fractions of the intracellular compartments are: myoplasm 68%, NSR 5.5%, JSR 0.32% and subspace 0.00041%, as proposed by Jafri et al. (1998).

The geometric parameters of the TATS were set to comply with the results of microscopic analysis of guinea-pig ventricular myocytes (Amsellem et al., 1995): fractional volume 2.9%, fractional area 52.6%, surface/volume ratio 13.5 μm^2 μm^{-3}. Applying these values in the model and assuming the mean tubule length (l_t) to be comparable to cellular radius (5.93 μm), the tubular membrane represents 5623 μm^2 (56.2 pF) and the surface membrane represents 5065 μm^2 (50.6 pF). All variables related to TATS and their values are given in Table A2 of Appendix 1 (see online supplementary material).

2.2. Distribution of ionic currents between the surface and tubular membranes

The fractions of individual ionic currents in the TATS were set using data mainly obtained from guinea-pig ventricular cardiomyocytes.

I_{Na}: Shepherd and McDonough (1998) investigated the rate of change of I_{Na} when bathing Na was altered, assuming that I_{Na} in the TATS would change more slowly than that at the cell surface because of diffusion delays. The best fit of model output with their experimental data was achieved when 57% of I_{Na} was assigned to the tubular membrane (Fig. 2A and section 2.6).

I_{CaL}: L-type Ca^{2+} channels are predominantly co-localized with ryanodine receptors at the dyads in the TATS, (see reviews by Scriven et al., 2000; Brette and Orchard, 2003; Brette et al., 2005a). This is consistent with 64% of I_{CaL} being restored with a slow time course after Ca^{2+} repletion in the external medium (Shepherd and McDonough, 1998). On the basis of these results we assigned 64% of this current to the tubular membrane, which was justified by the model simulations (Fig. 2B and section 2.6).

I_{Kr} and I_{Ks}: the rapid and slow components of delayed rectifier K^+ current have been reported to be preferentially located at the TATS membrane (Rasmussen et al., 2004). However, the majority of ERG (the protein underlying I_{Kr}) appears to be located near the mouth of the t-tubules (Rasmussen et al., 2004). We therefore assumed these channels to be uniformly distributed between the tubular and surface membranes.

I_{K1}: 83% of the inwardly rectifying K^+ current appears to be lost when rabbit cells lose their TATS with time in culture; furthermore, the onset of block by Ba^{2+} shows a sigmoid time course suggesting a diffusion delay (Christé, 1999). Immunohistochemical studies by Christé et al. (unpublished data, see fig. 6 in companion review (Pasek et al., 2007)) and Clark et al. (2001) support this view. 80% of this current was therefore assigned to the tubular membrane.

I_{NaCa}: Na-Ca exchange has been reported to be mainly located in TATS of guinea-pig (Frank et al., 1992) and rat (Yang et al., 2002; Thomas et al., 2003). However, Kieval et al., (1992) reported a more even distribution in both species. As no quantitative data are available for the guinea-pig, we have used uniform distribution of this current (52.6% in TATS) between the tubular and surface membranes.

I_{NaK}: Na-K pump immunolabelling suggests a uniform concentration in the tubular and surface membranes in guinea-pig cells (McDonough et al., 1996). The fraction of I_{NaK} in tubular membrane was therefore set to 52.6%. The possibility of two different Na-K ATPase isoforms (Gao et al., 1995) was ignored.

I_{pCa}: Ca^{2+} pump localisation determined using immunolabelling in guinea-pig myocytes suggests that it is found predominantly in the surface membrane and is scarce in the TATS (Iwata et al., 1994). We therefore assigned 20% of I_{pCa} to the TATS.

$I_{K(ATP)}$: A tail current can be recorded in guinea-pig cells following activation of the ATP sensitive K^+ current ($I_{K(ATP)}$) (Yasui et al., 1993; Tourneur et al., 1994) suggesting that K_{ATP}-channels are present in the TATS and cause K^+ accumulation. We have observed dense labelling of TATS by antibody against Kir6.2 channel subunit in rabbit ventricular cardiomyocytes (Christé et al., unpublished data, see fig. 6 in companion review (Pasek et al., 2007)). However, Korchev et al. (2000) recorded maximal $I_{K(ATP)}$ current density around the mouths of t-tubules using high resolution scanning patch clamp. In the absence of quantitative information about the distribution of K_{ATP} channels, we set uniform density of the K_{ATP} channels, resulting in 52.6% of $I_{K(ATP)}$ in TATS.

Data are unavailable for the distribution of the persistent Na^+ current (I_{Naps}), the plateau K^+ current (I_{Kp}), the non-specific Ca^{2+}-activated current (I_{nsCa}) and background currents (I_{Nab}, I_{Cab}), so their distribution was assumed to be uniform (52.6% in TATS) over the whole cell membrane.

The fractions of individual currents in the TATS are listed in Table 1, together with the maximum current, conductivity or permeability of transporters in surface and tubular membrane.

TABLE 1 NEAR HERE

Electrical properties of surface and tubular membrane transport systems used in the model.

2.3. Description of voltage and time-dependent properties of ion flux pathways

Although differences in Na^+ channel isoform (Brette et al., 2005b) and in the inactivation kinetics of I_{CaL} (Brette et al., 2005c) between surface and tubular membranes have been reported in rat ventricular myocytes, there is no evidence of such differences in guinea-pig ventricular myocytes. Thus, the ionic currents in both these membranes were described by the same set of equations, shown in Appendix 1 (see online supplementary material); some were reformulated on the basis of new experimental data from guinea-pig whereas others were adopted from existing models.

I_{Na}: The classical Hodgkin-Huxley formalism with three activation gates (m^3) and one inactivation (h) gate was used to describe I_{Na}. The voltage dependencies of steady state activation ($\overline{m}$), steady state inactivation ($\overline{h}$) and the related time constants (τ_m, τ_h) were derived from the experimental data of Li et al. (2002) obtained at 16 °C. To simulate the behaviour of I_{Na} at 37°C the voltage dependence of $\overline{m}$ and $\overline{h}$ were shifted by +9 mV (Nagatomo et al., 1998) and the rate of channel gating was increased by a factor 4.83 (Taniguchi et al., 1994; Nagatomo et al., 1998). To reproduce experimental data more closely, the decreased reversal potential (E_{Na}) was simulated by introducing a 10.7% permeability of the channel to K^+ (Nordin, 1993). However, transfer of K^+ through Na-channels was not introduced into the model equations. The maximum channel conductance (g_{Na}) was set to 30 mS μF^{-1} to generate the maximum upstroke velocity $(dV/dt)_{max}$ = 512 V s^{-1} observed by Taniguchi et al. (1994) in guinea-pig myocytes.

I_{Naps}: The persistent Na^+ current was formulated according to the description and experimental data of Sakmann et al. (2000). To comply with their experimental estimate of 33.5 mV for the reversal potential of I_{Naps} (E_{Naps}) we adopted the same reversal potential as for I_{Na} ($E_{Naps} = E_{Na}$).

I_{CaL}: The function of I_{CaL} channels is described by the multi-state model of Jaffri et al. (1998). The voltage dependent inactivation at steady state was, however, modified to exhibit a sigmoid relationship (Findlay, 2002) and realistic action potential (AP) configuration (Wang et al., 1988; Grantham and Cannell, 1996). The channel permeability was lowered to 0.0048 cm s^{-1} (as compared with 0.0054 cm s^{-1} proposed by Jafri et al. (1998)) to prevent intracellular Ca^{2+} overload at high stimulation frequencies.

I_{Kr} and I_{Ks}: The formulations for these currents were adopted from Zeng et al. (1995). The conductances were adjusted to ensure a realistic action potential duration compared to those observed in guinea-pig at 36 - 37 °C (Wang et al., 1988).

I_{Kp}, I_{K1}, $I_{K(Na)}$, $I_{K(ATP)}$, $I_{ns(Ca)}$, I_{NaCa}, I_{NaK}, I_{pCa} and background currents: the description of these currents was adopted from the model of Faber and Rudy (2000). However, some minor changes in current parameters were used (see Appendix 1 as online supplementary material) to prevent intracellular Ca^{2+} and Na^{+} overload at high stimulation frequencies (up to 6 Hz) and to ensure experimentally observed levels of all intracellular ionic concentrations at rest.

To observe the charge conservation principle described by Hund et al. (2001) and to ensure long-term stability of the model, we incorporated the stimulus current (-4.8 nA, 1 ms) into the equation controlling intracellular $[K^{+}]$.

2.4. Electrical interaction between surface and tubular membrane

The TATS was described as a single compartment separated from the surface membrane, and connected to the bulk peri-cellular solution by the mean resistance of the tubular system (R_{st}; Fig. 1B). The contribution of one tubule to R_{st} was expressed as the resistance of a cylindrical conductor whose length, radius and specific resistance corresponded to half of the tubular effective length ($l_t/2$), its average radius (r_t), and the specific resistance of the extracellular solution (ρ_{ext}), respectively. (For Tyrode solution, $\rho_{ext} \approx 83.33$ Ω cm). Electrically the TATS represents a parallel combination of all (n_t) tubules in the model cell, so that the mean resistance of the tubular system can be calculated from the relation

$$R_{st} = \rho_{ext}\, l_t / (2\, \pi\, r_t^2\, n_t). \qquad (1)$$

Assuming the specific intracellular resistance to be three times higher ($\rho_{int} \approx 253$ Ω cm (Daut, 1982; Cooklin et al., 1998)) than Tyrode solution, and given the significantly larger effective section of the intracellular conducting pathway, the intracellular resistance can be considered insignificant and was neglected. Therefore, the cell interior was regarded as an equipotential space connected with the pipette resistance R_{el}.

As follows from the electrical equivalence circuit shown in Fig. 1B the stimulating current I_m equals the sum of the surface membrane current I_{ms} and the current through the TATS I_{mt}:

$$I_m = I_{ms} + I_{mt}. \qquad (2)$$

In current clamp conditions I_m = 0 throughout except for the duration of the short (1 ms) suprathreshold stimulus. It follows that a common current circulates through both membrane systems, named circulation current (I_{circ}):

$$I_{circ} = I_{ms} = -I_{mt} = (V_{ms} - V_{mt}) / R_{st} \quad (3)$$

In voltage clamp conditions the current I_m can be expressed in terms of the voltage drop across the series resistance (R_{el}):

$$I_m = (V_c - V_{ms})/R_{el}, \quad (4)$$

where V_c denotes the imposed voltage.

2.5. Intracellular Ca^{2+} handling

The description of intracellular Ca^{2+} handling consists of equations controlling the free Ca^{2+} concentrations in the subspace ($[Ca^{2+}]_{ss}$), intracellular space ($[Ca^{2+}]_i$) and sarcoplasmic reticulum compartments ($[Ca^{2+}]_{NSR}$, $[Ca^{2+}]_{JSR}$). The whole process, including intracellular Ca^{2+} transport and Ca^{2+} buffering by troponin (B_{htrpn}, B_{ltrpn}), calmodulin (B_{cm}) and calsequestrin (B_{cs}), was adopted from the model of Jafri et al. (1998). The maximum Ca^{2+} pump rate of the SR Ca^{2+}- ATPase, Ca^{2+} leak rate from the NSR into the myoplasm and the rate of transition between P_{c1} and P_{o1} states of the JSR Ca^{2+} release channel were adjusted (see Appendix 1 as online supplementary material) to simulate a Ca^{2+} transient similar to that observed in guinea-pig (Siri et al., 1991).

2.6. Ionic diffusion between tubular and extracellular space

We used our model to reproduce the experimental conditions and protocols of Shepherd and McDonough (1998). In these simulations, the model was supplemented by an external compartment representing fast ion exchange ($\tau_{Na,e}$, $\tau_{Ca,e}$, $\tau_{K,e}$) between a perfusion pipette and an external compartment near the peripheral cell membrane. The experimentally observed changes of I_{Na} upon changing bath $[Na^+]$ from 150 to 105 mM were approximated by these authors by a double exponential function with a fastly decaying phase of 36% of the maximal change (time constant of 24 ms), attributed to changes in $[Na^+]$ in the external compartment. The remaining 64% decayed with a time constant of 230 ms was attributed to changes in $[Na^+]$

concentration in the TATS lumen. However, the best fit of the model output with their data (Fig. 2A) required that the fraction of I_{Na} in the TATS was set to 0.57 and the time constant of Na^+ exchange between the TATS and the external compartment ($\tau_{Na,t}$) was set to 214 ms whereas that between the external compartment and the bath ($\tau_{Na,e}$) was set to 22 ms. To reproduce the changes in I_{CaL} measured by Shepherd and McDonough upon changing bath [Ca^{2+}] from 0.45 to 1.8 mM (i.e.: 36% of the change being restored with a time constant of 22 ms, and the remaining 64% with a time constant of 195 ms) (see Fig. 2B), required that the fraction of I_{CaL} in the TATS was set to 0.643 and the time constants $\tau_{Ca,t}$ and $\tau_{Ca,e}$ were set to 236 ms and 24 ms respectively. These results suggest that experimental measurements of peak currents are not a linear image of changes in concentrations, probably because of a non linear relation to external ion concentration (see Figure 2 in (Shepherd and McDonough, 1998)). The changes in holding current upon a change in bath [K^+] were consistent with a $\tau_{K,t}$ at 200 ms.

The final values used in the model were $\tau_{Na,t} = \tau_{K,t} = 200$ ms, and $\tau_{Ca,t} = 240$ ms and the fractions of 0.57 and 0.64 of respectively I_{Na} and I_{Ca} in the TATS (see Table A7 in Appendix 1 as online supplementary material). The model with these settings is termed the "basic model" in the following text.

FIGURE 2 NEAR HERE

Model reconstruction of Shepherd and McDonough's experiment.

A) Na^+-diffusion B) Ca^{2+} -diffusion

However Blatter and Niggli (1998), using a membrane-bound Ca^{2+} indicator, reported that wash-out of Ca^{2+} from the TATS of guinea-pig ventricular myocytes occurred with a $t_{1/2}$ of 0.9 s at the surface and 1.7 s in the deeper regions of the TATS. Assuming a single exponential time course of decrease of $[Ca^{2+}]_t$ the corresponding time constants are 1.3 s and 2.46 s. This is slower than the value derived from I_{CaL} measurements (Shepherd and McDonough, 1998). The reasons for the discrepancy are not clear. Therefore, in some of the computations, the shortest time constant estimated from Blatter and Niggli's data (1.3 s) was used, to investigate whether this would affect the results.

2.7. Numerical integration technique

The model was implemented using MATLAB 6.5 (The MathWorks, Inc., Natick, MA) and the numerical computation of the system of 54 non-linear differential equations was performed using the solver for stiff systems ODE-15s. The model equations were simultaneously solved using a time step adjusted to keep the estimated relative error of inner variables below a threshold value of 0.001. After every change in the model equations or parameter values, the model was run for 3 hours of equivalent cell time to ensure that steady-state was reached. The values of all variables at this time were assigned as starting values before running model trials.

3. Results

3.1. Validation of the model

Long term stability

The stability of the model at rest was tested in current clamp without stimulation (see Methods). Fig. 3 shows that intracellular ion concentrations were stable during 3 simulated hours of quiescence. Fig. 3 also shows the ability of the model to return to resting steady-state values after 1 hour of stimulation at 4 Hz and after a brief exposure to low extracellular $[K^+]$.

Fig. 3 NEAR HERE
Stability of the model with time

During 4 Hz stimulation, intracellular $[Na^+]$ increased from 8.08 to 13.04 mM and end-diastolic $[Ca^{2+}]$ from 37 to 205 nM. Intracellular K^+ concentration decreased slightly (by 4% from 140 to 134.3 mM) and end-diastolic membrane potential depolarised from -85.5 to -84.1 mV. Activity also increased the end-diastolic tubular concentrations of Ca^{2+} (from 1.79 to 1.82 mM) and K^+ (from 5.46 mM stabilising to 5.5 mM). All of these values were close to steady state within 6 minutes of stimulation. Upon cessation of stimulation, despite transient changes in some of these variables, all returned within ~6 minutes to near the resting-state values before stimulation. After 1 minute of exposure to low extracellular $[K^+]$ (0.5 mM), all values underwent changes that were rapidly reversed. After each of the 3-hour stabilisation periods at rest (at 180, 420 and 600 minutes), all variables in the model had returned to values that differed from the initial values (at 0 minute) by less than 0.2%.

Action potential and membrane currents during changes of stimulation frequency

Fig. 4 shows the decrease in steady-state action potential duration and the changes in action potential configuration generated by the model as stimulation frequency was increased from 1 Hz to 2, 3, 4, and 5 Hz (right panel); these are similar to the changes in action potential configuration recorded in guinea-pig papillary muscles by Wang et al. (1988) when stimulation frequency was increased over this range (Fig. 4, left).

Fig. 4 NEAR HERE

Action potentials as compared with those from GP cells

The systolic Ca^{2+} transient and the changes in membrane currents underlying the altered action potential configuration at different stimulation rates are shown in Fig. 5, and the key numerical values in Table 2. Increasing stimulation rate increased end-diastolic $[Ca^{2+}]_i$ and $[Na^+]_i$ whereas it decreased end-diastolic $[K^+]_i$ (not shown). Action potential shortening was caused by a decrease of I_{CaL} due to cumulative inactivation, by an increase of I_{Kr} and I_{Ks} in the early plateau phase, and partly by an increase of outward I_{NaCa} (Egan et al., 1989) and I_{NaK}.

The size of the currents flowing across the surface and tubular membranes reflect the distribution of ion flux pathways between the two membranes (Table 1). However, this is not the sole determinant of the size of the tubular currents, which are also modulated by changes of ion concentrations within the TATS lumen (see below). The next series of simulations was designed to investigate the electrical properties of tubular and surface membranes.

Fig. 5 NEAR HERE

APs and currents in the model cell

Table 2 NEAR HERE

AP durations and intracellular concentrations at steady state in the model run at various frequencies.

3.2. The electrical properties of tubular and surface membranes

Passive electrical properties of the model cell

In principle, the capacitance of the tubular membrane may be charged more slowly than that of the surface membrane because of the tubular series resistance R_{st}, which would result in bi-exponential decay of the capacitance current. However, in agreement with morphological data, the estimated value of R_{st} (35.18 kΩ) is at least one order of magnitude smaller than the electrode resistance R_{el} even after realistic compensation for series resistance. The time course of current in response to a small voltage step (V_c) from resting voltage can be estimated

analytically using the simplified model (Fig. 6A) in which ionic transport is described by the resistances of the surface and tubular membranes R_{ms} = 67 MΩ and R_{mt} = 18 MΩ calculated as minimum chord resistances in the range of membrane voltage -85 ± 10 mV from the complete model (Fig. 1B).

Analysis of the circuit represented in Fig. 6A leads to the expression of the input current in response to a step of input voltage as a sum of two exponentials and a constant: $I_m = I_1 . exp(-t/\tau_1) + I_2 . exp(-t/\tau_2) + I_o$. A complete description of this analysis is provided in Appendix 2 (as online supplementary material). Assuming electrode resistance R_{el} = 0.5 MΩ, then τ_1 = 52.6 µs, τ_2 = 0.92 µs, $I_2/I_1 \approx 0.02$ and $I_o/I_1 \approx 0.06$. Only the first component with the longer time constant τ_1 is significant and the time course of the recorded current appears mono-exponential as illustrated in Fig. 6B and D.

The voltages at the tubular and surface membranes (V_{mt} and V_{ms}) are expressed as $V_{ms} = V_{s1} . exp(-t/\tau_1) + V_{s2} . exp(-t/\tau_2) + V_{so}$ and $V_{mt} = V_{t1} . exp(-t/\tau_1) + V_{t2} . exp(-t/\tau_2) + V_{to}$ with identical time constants and similar ratios of the magnitudes of components as for the input current. The difference in voltage between the surface and tubular membranes is negligible as shown in Fig. 6C.

The results of this analytical solution were confirmed by numerical simulations using the whole model cell with TATS (Fig. 6D and E). A 10 mV hyperpolarizing pulse was applied from a holding potential near the zero-current voltage (-85 mV). The decay of the current (squares) was fitted with either a single exponential or the sum of 2 exponentials, both with offset. These fits, superimposed in Fig. 6D, are practically congruent. The time courses of changes in voltage at tubular and surface membranes in the model (Fig. 6E) are very similar to theoretically computed ones (Fig. 6C).

Fig. 6 NEAR HERE

Passive properties of the cell with TATS

The results of these simulations are consistent with experimental data showing a single exponential decay of the whole cell capacitance current obtained using small voltage steps (Brette and Orchard, unpublished data).

Voltage at the tubular and surface membranes during cellular activity

It has long been speculated that voltage control within the TATS may be inadequate in voltage clamp experiments, allowing voltage escape. Using the electrical equivalence scheme of the cellular membrane systems (Fig. 1B) the voltage difference between the tubular and the surface membranes can be estimated as:

$$\Delta V_{s,t} = V_{ms} - V_{mt} = R_{st} I_{mt}.$$

When $R_{st} = 35$ kΩ, it is apparent that $\Delta V_{s,t}$ does not exceed 0.9 mV even at the maximum tubular I_{Na} of ≈38 nA ($I_{mt} \approx 24.5$ nA). Under normal conditions, other ionic currents remain below 3.3 nA suggesting negligible $\Delta V_{s,t}$ (≤ 120 μV). Simulation of a voltage clamp experiment (a 75 mV depolarising pulse applied from a holding voltage of –85 mV, with electrode resistance set at 0.5 MΩ; Fig. 7A) shows that membrane voltage overshoots the command potential by 19 mV at peak I_{Na} and 2.64 mV at peak I_{CaL} (Fig. 7A middle panel). Corresponding $\Delta V_{s,t}$ were 0.86 mV and 0.117 mV (Fig. 7A lower panel). Thus membrane voltage was almost homogeneous over the whole cell membrane, and the lack of control of membrane voltage was almost entirely due to pipette series resistance.

In current clamp, $\Delta V_{s,t}$ was even smaller than in voltage clamp. Action potentials were generated at 4 Hz in the model by applying a stimulation pulse of 4.8 nA for 1 ms to the surface membrane. Fig. 7B shows that action potentials generated at both membranes are indistinguishable at the usual scale; $\Delta V_{s,t}$ shown at higher gain in Fig. 7B (lower panel) is less than 190 μV throughout the action potential. Thus the model suggests that membrane potential is also highly homogeneous across the whole cell membrane in current clamp.

Fig. 7 NEAR HERE

Voltage homogeneity in voltage clamp and in current clamp

However, these results do not imply that the effects of the tubular system on the AP are insignificant. The homogeneity of the membrane voltage is the result of tight electrical coupling between the two membranes. Fig. 8 shows that APs generated by the surface and tubular membranes are quite different if their electrical coupling is disconnected (continuous lines). Due to the tight coupling, the resulting common AP falls between the surface and tubular APs (dotted line). It follows that any disruption of electrical coupling between the

membrane systems due to pathological processes would shorten the AP generated by the surface membrane (see also Fig. 2 and chapter 7 of the accompanying review (Pasek et al., 2007)). An increased gradient of AP duration between normal and pathological regions is a known arrhythmogenic factor.

Fig. 8 NEAR HERE

Differences between APs generated by isolated tubular and surface membranes

3.3. Changes of tubular ion concentrations during cellular activity

Ion flux across the tubular membrane, coupled to slow diffusion between the TATS lumen and the extracellular space might lead to changes in lumenal ion concentrations. This could be important since such changes would, in turn, alter ion flux across the tubular membrane. We therefore used the model to investigate whether significant changes in lumenal ion concentrations occur.

At resting steady state, tubular [Ca^{2+}] (1.79 mM) was lower by 0.55% and tubular [K^+] (5.46 mM) was higher by 1.1% than extracellular [Ca^{2+}] (1.8 mM) and [K^+] (5.4 mM), respectively. Resting membrane voltage V_{mt} was -85.5364 mV and V_{ms} was -85.5361 mV, i.e. a 0.3 μV difference. These differences result from different densities of ion pathways in the tubular and surface membranes. Consequently, both membrane systems show different resting voltages if disconnected: V_{mt} = -85.99 mV and V_{ms} = -84.48 mV. This 1.5 mV difference is dissipated by coupling through R_{st}. The equalising current (I_{circ} = 8.53 pA, equation 3) in conjunction with restricted diffusion to and from the extracellular solution causes small deviations of tubular ionic concentrations from extracellular levels even at rest.

Fig. 9 NEAR HERE

Changes of tubular ionic concentrations during cellular activity

Fig. 9 shows that during activity ion fluxes and restricted diffusion induce cyclic changes of [Ca^{2+}], [K^+] and [Na^+] (panels A-C) within the TATS lumen during each action potential, which result in the time-averaged concentrations of these ions being lower (Ca^{2+}, Na^+) or higher (K^+) than their resting values. During simulation of action potentials at 1 Hz, $[K^+]_t$ and

$[Na^+]_t$ increase by 4% and 0.19% respectively, while $[Ca^{2+}]_t$ decreases by 13.8% from the corresponding extracellular ion concentrations. The changes in ion concentrations within the TATS lumen are frequency dependent: panels D-F of Fig. 9 show the range of deviations of $[Ca^{2+}]_t$, $[K^+]_t$ and $[Na^+]_t$ from extracellular values, determined at steady state during stimulation at frequencies between 1 and 6 Hz.

Blatter and Niggli (1998) showed washout of tubular Ca^{2+} in guinea-pig myocytes with $t_{1/2}$ = 0.9 s ($\tau \approx 1.3$ s) at the outer region of TATS, and 1.7 s ($\tau \approx 2.46$ s) in the deeper regions of TATS. This suggests that tubular Ca^{2+} diffusion could be slower than in our basic model (τ_{Ca} = 0.24 s, derived from Shepherd and McDonough's data (1998)). We therefore investigated the effect of increasing the time constant of Ca^{2+} exchange between the extracellular solution and the TATS from 0.24 to 1.3 s; the shortest delay observed by Blatter and Niggli (1998).

Table 3 NEAR HERE

Concentration changes in TATS at steady state at various frequencies

Table 3 shows the peak accumulation and depletion of Ca^{2+} within the TATS during a single steady-state cycle ($\Delta[Ca^{2+}]_t$) at different stimulation frequencies in the basic model (Table 3A), and in the model with slower Ca^{2+} diffusion (τ_{Ca} = 1.3 s; Table 3B). Although the amplitude of the changes of $[Ca^{2+}]_t$ is only slightly affected, the average tubular Ca^{2+} concentration was significantly reduced in the second case. The changes in tubular $[K^+]$ were not affected by this modification.

3.4. Consequences of ionic concentration changes in tubular system

The data in the previous section show that during activity, tubular $[Ca^{2+}]$ and $[K^+]$ differ markedly from those in the bulk extracellular solution, whereas the changes of tubular $[Na^+]$ are negligible. These changes arise from the flow of ions through ion flux pathways located within the TATS. These ion flux pathways will, in turn, be exposed to the altered ion concentrations, which may, therefore, have marked effects on tubular membrane currents and hence intracellular ion concentrations. The subsequent simulations were designed to test these ideas, and to delineate the roles played by changes of $[Ca^{2+}]$ and $[K^+]$ in the TATS lumen.

Effects of changes of tubular ion concentrations on ionic currents

To test the idea that activity-dependent changes of ion concentrations in the TATS modulate tubular membrane currents, we compared simulations from the basic model with those in which the ion concentrations in the TATS were suddenly fixed at extracellular levels. Fig. 10 shows superimposed traces of $I_{CaL,t}$, $I_{NaCa,t}$ and $I_{K1,t}$ computed for both cases in response to a 200 ms voltage pulse from resting voltage (-85.54 mV) to +20 mV (Fig.10A) and during an AP elicited from resting state (Fig. 10B). When compared with the model with fixed tubular ion concentrations, the results from the basic model show the consequences of tubular Ca^{2+} depletion and K^+ accumulation: $I_{CaL,t}$, $I_{K1,t}$ and outward $I_{NaCa,t}$ are reduced.

Fig. 10 NEAR HERE

Effect of changes of tubular ion concentrations on tubular ionic currents.

Table 4 NEAR HERE

Changes in charge as due to concentration changes in TATS.

V clamp and AP from rest.

To appreciate the impact of this modulation on transmembrane ion transfer, the currents shown in Fig. 10 were integrated. The amount of charge transferred during 1 s from the onset of the pulse or the AP when the ion concentrations in the TATS were fixed or allowed to change is shown in Table 4. During the voltage clamp pulse, the amount of charge transferred by $I_{CaL,t}$ and by $I_{K1,t}$ was markedly reduced (by 15.3 and 27% respectively) when ion concentrations were allowed to change, showing that Ca^{2+} depletion and K^+ accumulation have marked modulating effects. However, the net inward charge transferred by $I_{NaCa,t}$ was only slightly increased. During an action potential, the decrease of charge transfer via $I_{CaL,t}$ and $I_{K1,t}$ was markedly less (by 8 and 9.6% respectively) than observed under voltage clamp. Thus the changes observed under voltage clamp may not be a good predictor of those that occur during an action potential.

A similar analysis was carried out during steady state stimulation at 1, 4 and 6 Hz in current clamp conditions. Table 5 summarises the effect of tubular ion concentration changes on charge transferred by $I_{CaL,t}$, $I_{NaCa,t}$, $I_{K,t}$ (sum of $I_{Kr,t}$ and $I_{Ks,t}$) and $I_{K1,t}$ during one cycle in the basic model (Table 5A) and in the model with slower Ca^{2+} diffusion (Table 5B) as described in

the previous section. Except for $I_{NaCa,t}$, the activity-related changes of tubular ion concentrations in the basic model caused reduction of transferred charges in a frequency dependent manner. This effect was significantly enhanced when the longer time constant of Ca^{2+} exchange between the TATS and extracellular space was used (Table 5B).

Table 5 NEAR HERE

Changes in charge transferred as due to concentration changes in TATS. APs at steady state.

Effects of changes of tubular ion concentrations on intracellular Ca^{2+} load

The data in the previous section suggest that changes of tubular ion concentrations alter ion flux across the tubular membrane. While $I_{Ca,s}$ and $I_{NaCa,s}$ were only slightly affected (secondary to a minute change of AP), Ca^{2+} influx via $I_{CaL,t}$ was significantly decreased and net Ca^{2+} extrusion via $I_{NaCa,t}$ was increased. This suggests that Ca^{2+} depletion in the TATS would tend to decrease intracellular Ca^{2+} load.

Fig. 11 NEAR HERE

Effect of changes of tubular ion concentrations on Ca^{2+} load in NSR at three stimulation frequencies.

To test this idea, NSR Ca^{2+} load and the systolic Ca^{2+} transient were compared in the basic model and the model with slower tubular Ca^{2+} diffusion, when tubular ion concentrations were fixed or allowed to change (Fig. 11). At steady state, the simulations that allowed tubular ion concentrations to change exhibited lower NSR Ca^{2+} load and smaller Ca^{2+} transients than the simulations in which tubular ion concentrations were maintained at extracellular levels. The effect depended on stimulation frequency and on the time constant of Ca^{2+} exchange between the TATS lumen and extracellular space. In the basic model the end-diastolic level of $[Ca^{2+}]_{NSR}$ was lower by 6%, 4.4%, and 4.6% at 1 Hz, 4Hz, and 6 Hz, respectively. In the model with slower Ca^{2+}diffusion (τ_{Ca} = 1.3 s) the corresponding reductions were 9.8%, 12.2%, and 13.5%. The Ca^{2+} transients were affected accordingly. This effect was caused predominantly by decreased Ca^{2+} influx via I_{CaL} and by increased Ca^{2+} extrusion via I_{NaCa} as a consequence of tubular Ca^{2+} depletion (Table 5).

The participation of tubular K^+ accumulation in this effect was explored by a simulation in which changes of $[K^+]_t$ were allowed, but tubular $[Ca^{2+}]$ and $[Na^+]$ were fixed at extracellular levels. The Ca^{2+} load of NSR in the basic model at 4 Hz was reduced by 1.07% indicating that tubular K^+ accumulation was responsible for almost a quarter of the 4.4% reduction (results not shown).

Fig. 12 NEAR HERE

Effect of changes of tubular ion concentrations on Ca^{2+} load in NSR at 1 Hz stimulation.

Resting steady-state tubular ion concentrations are almost identical in simulations with fixed or variable lumenal ion concentrations (Fig. 9). Thus, negligible differences of $[Ca^{2+}]_{NSR}$ would be expected in the two conditions after a long rest. Superimposed changes of $[Ca^{2+}]_{NSR}$ during stimulation at 1 Hz from resting steady-state are illustrated in Fig. 12. In all three models net Ca^{2+} influx was similar during the first cycle (~0.19 fmol). $[Ca^{2+}]_{NSR}$ increased in subsequent cycles, while net Ca^{2+} influx was declining to zero, with different rates of decay, so that different dynamic steady-states were achieved in each condition.

These results suggest that: (i) changes of ion concentration in the TATS lumen can modulate SR Ca^{2+} load and consequently the systolic $[Ca^{2+}]_i$ transient; (ii) the reduction of intracellular Ca^{2+} content due to changes of tubular ion concentration increases with stimulation rate in the range of physiological frequencies; (iii) the impact of the TATS on the inotropic status of the guinea-pig ventricular cell depends significantly on the rate of Ca^{2+} diffusion between the tubular and extracellular space.

4. Discussion

Recent experimental work has demonstrated the importance of the TATS in cardiac cell function (Brette and Orchard, 2003). Immunohistochemical and functional studies have shown that key proteins involved in cardiac cell function, in particular excitation-contraction coupling, are located predominantly at the TATS membrane. This concentration of ion flux pathways, coupled to a restricted intracellular diffusion ("fuzzy") space, and restricted ionic diffusion into the TATS lumen, suggests that the transmembrane ion gradient to which these ion transport proteins are exposed may be different from that determined from extracellular and intracellular ion measurements. The magnitude and hence the importance of such effects is currently

difficult to ascertain experimentally; however computer models enable the possible importance of such effects to be determined.

4.1. The functional role of TATS in cardiac cell

Electrical properties of the tubular membrane

One obvious question that could be addressed is whether the surface and tubular transmembrane voltages differ at rest and during activity.

The only difference between the two membranes in the present model is the concentration of ion flux pathways. Other properties were assumed identical. The present model assumes a single compartment of short, unbranched tubules. Although the cable properties of cardiac TATS have not been evaluated, the maximum length of the t-tubules (25 μm in rat (Soeller and Cannell, 1999)); is much lower than their space constant ($\lambda_t \cong (r_m / r_t)^{\frac{1}{2}}$) of 240 μm at rest, assuming a specific membrane resistance of 6.7 kΩ cm^2 (Daut, 1982) and a specific resistivity of the extracellular solution of 83.33 Ω cm. Thus the TATS may be uniformly polarised in current- and voltage-clamp. Our theoretical analysis (Appendix 2 and Fig. 6A and 6B-C) and simulations using the model (Fig. 6C-D) agree with this idea. The charging of tubular versus surface membrane capacitance is delayed by less than 4 μs (Fig. 6C and E), consistent with the experimentally observed single exponential capacitance charging current of a ventricular cardiac myocyte. Furthermore, with maximal membrane current in voltage clamp (Fig. 7A), the difference in membrane voltage between the TATS and surface membranes is less than 1 mV, and less than 190 μV during an action potential (Fig. 7B). This is due to tight electrical coupling through R_{st} and negligible intracellular resistance, which cancels voltage differences (Fig. 8). For these reasons, the entire cell membrane behaves, electrically, as a uniform whole.

The effect of ion flux across the tubular membrane combined with limited ion diffusion

It has been recognised for many years that in multicellular preparations of cardiac muscle, trans-sarcolemmal ion fluxes can lead to local accumulation and depletion of ions in inter-cellular clefts, and that this could have effects on membrane currents and hence cell function (Attwell et al., 1979). However, the possibility that ion accumulation or depletion in the TATS may alter local currents across the tubular membrane has been less fully considered, although

such changes might have important consequences, in particular for excitation-contraction coupling.

The present work supports this idea. Fig. 9 shows that during activity, tubular [Ca^{2+}] decreases and subsequently increases, while tubular [K^+] increases and subsequently declines during the latter part of the cycle. Changes of tubular [Na^+] also occur, but are negligible relative to the high extracellular [Na^+]. Depending on the rate of stimulation and the rate of ion diffusion between tubular lumen and extracellular space the maximum deviations of tubular ion concentrations from their bulk extracellular levels ranged between 7% and 20% for $[Ca^{2+}]_t$ and between 3% and 4% for $[K^+]_t$. These changes were sufficient to modulate currents flowing via Ca^{2+} and K^+ flux pathways in the TATS during an action potential (Fig. 10); the charge carried by $I_{CaL,t}$, $I_{Ks,t}$+$I_{Kr,t}$ and $I_{K1,t}$ was reduced, whereas the net outward transfer of Ca^{2+} by $I_{NaCa,t}$ was increased. The final consequence of this modulation was the decrease of SR Ca^{2+} load, and hence reduction of the systolic Ca^{2+} transient (Fig. 11).

There are conflicting published estimates of the fraction of Na-Ca exchange present in tubular membrane (see Material and methods). However when we considered a greater fraction (70%) of I_{NaCa} in tubular membrane, these effects were only slightly affected, suggesting that this distribution is not critical to the observed responses.

It should also be noted that the larger time constant for Ca^{2+} exchange between tubular lumen and extracellular space (1.3 s) used in the modified model was in the lower range of values reported by Blatter and Niggli (1998), since measured delays varied more than 3 fold from myocyte to myocyte, and longer delays were present in more central TATS. Thus the present model probably represents a minimum effect of TATS on the SR Ca^{2+} load and systolic Ca^{2+} transient.

Species differences

The guinea-pig model, in common with a model of the rat myocyte (Pasek et al., 2006), showed ion concentration changes in the TATS during stimulation that reduced the intracellular Ca^{2+} load and consequently the systolic Ca^{2+} transient. However, the magnitude of this effect and its frequency dependence differed markedly. In the basic guinea-pig model, concentration changes in the TATS lumen resulted in reduction of the steady-state Ca^{2+} transient by 3.5% at 1 Hz and 5.5% at 6 Hz. If the time constant for Ca^{2+} exchange between the TATS lumen and the extracellular solution was increased to 1.3 s, these values increased

to 5.7% and 15.2%, respectively. In the rat model, the frequency dependence was much more marked: only 2.8% at 1 Hz, but increasing to 24.4% at 5 Hz ($\tau_{Ca,t}$ = 500 ms). These differences are due to the different frequency dependencies of $[Ca^{2+}]_t$ changes. In the rat model, the maximum calcium depletion during a cycle increases with stimulation rate (Pasek et al., 2006) whereas it decreases in the basic guinea-pig model (Fig. 9). Thus, at physiological frequencies, the ion concentration changes in TATS appear to play more important role in rat than in guinea-pig myocytes.

There are two main factors underlying these differences: first, unlike in rat myocytes, the magnitude of I_{CaL} and action potential duration decrease with stimulation frequency in the guinea-pig (Wang et al., 1988; Bates and Gurney, 1999); second, the fraction of I_{CaL} in the TATS, which is responsible for tubular Ca^{2+} depletion, is lower in the guinea-pig (64%, Shepherd and McDonough, 1998) than in the rat (87%, Brette and Orchard, 2003).

4.2. Limitations of the model

Homogeneous distribution of ion transfer mechanisms within the TATS

In the present study, ion flux pathways were homogeneously distributed throughout the TATS. However Ca^{2+} channels appear to be concentrated at the dyads (Thomas et al., 2003). It has also been suggested (Lu et al., 2005) that to account for the detailed spatial features of EC coupling, Ca^{2+} handling proteins need to be 6-fold more concentrated in the TATS than in the surface membrane, and that the concentration of L-type calcium channels within the "deepest" parts of the TATS needs to be ~2.3-fold higher than in its peripheral parts. In addition, Na-Ca exchange appears to be absent from the longitudinal tubules (Thomas et al., 2003). Localised concentration of ion flux pathways would result in larger local changes of ion concentrations within the tubule lumen, and hence larger effects on membrane currents. In support of this idea, we have previously shown that local clustering of Ca^{2+} channels caused a profile with enhanced depletion near the channel clusters. Due to Ca^{2+} diffusion along the tubules, the local increases in Ca^{2+} depletion disappeared with time, so that within ~150 ms, the profile became similar to that observed with uniform Ca^{2+} channel distribution (Simurda et al., 2004). At early times during an action potential, this additional Ca^{2+} depletion may cause larger changes in the time course of the action potential and ion fluxes than under the assumption of uniform distribution. Thus, neglecting inhomogeneous distribution of Ca^{2+}

channels and possibly of Na-Ca exchange may lead to underestimation of the consequences of Ca^{2+} depletion in the present model.

Representation of dyadic junctions and SR into a single lumped ensemble

In the present model, the dyads and SR have been lumped into single structures (dyadic subspace, junctional SR and network SR) where each represents the sum of respective compartments over the whole cell (Fig. 1). This ignores regional differences, such as the lower efficiency of peripheral versus tubular EC-coupling (Brette et al., 2006), and thus hinders attempts to account in detail for the role played by surface and TATS dyads in EC coupling. Furthermore, the reduced entry of Ca^{2+} from the TATS dyads into the common subspace, following Ca^{2+} depletion in the TATS lumen, is averaged with unchanged Ca^{2+} entry at peripheral dyads. This attenuates the moderating effect of Ca^{2+} depletion in TATS on SR Ca^{2+} release. Thus the functional consequences of ion concentration changes in TATS are likely to be underestimated in the present model.

Another limitation is the lack of data on the distribution of several ion flux pathways between the tubular and surface membranes (Table 1). In such cases, we have assumed a uniform distribution, which may be inaccurate. However, the major pathways controlling Ca^{2+} fluxes have been assigned documented distributions.

Absence of limited diffusion in intercellular clefts

In this paper we explored the functional consequences of ion concentration changes in TATS in a model of a single cardiac cell, without restricted ion diffusion in intercellular clefts, which was considered by Hilgemann and Noble (1987). Changes in these clefts may mirror ion concentration changes in the TATS lumen, although with substantially lower amplitude, and may modulate the changes occurring in the TATS.

In spite of its limitations, this guinea-pig model suggests that ion concentration changes in the TATS lumen are sufficiently marked to modulate the function of the ventricular myocyte. If confirmed experimentally, this may contribute to fuller understanding of ventricular cell function.

Acknowledgements

This study was supported by the project AV0Z 20760514 from the Institute of Thermomechanics of Czech Academy of Sciences, by the project MSM 0021622402 from the Ministry of Education, Youth and Sports of the Czech Republic, and by the Wellcome trust and the British Heart Foundation. M. Pásek was granted a Junior Fellowship of the Physiological Society and G. Christé was awarded a research grant from the Fédération des Maladies Orphelines, France.

References

Amsellem, J., Delorme, R., Souchier, C., Christé, G., Bernengo, J. C., Ojeda, C., 1994, 3D reconstruction of transverse tubular membrane system in guinea-pig cardiac ventricular cells: its possible implication in K^+ accumulation-depletion phenomena: ICEM, 13, 183-184.

Amsellem, J., Delorme, R., Souchier, C., Ojeda, C., 1995. Transverse-axial tubular system in guinea pig ventricular cardiomyocyte: 3D reconstruction, quantification and its possible role in K^+ accumulation-depletion phenomenon in single cells. Biol. Cell 85, 43-54.

Attwell, D., Cohen, I., Eisner, D., 1979. Membrane potential and ion concentration stability conditions for a cell with restricted extracellular space. Proc. R. Soc. Lond. 206, 145-161.

Bates, S.E., Gurney, A.M., 1999. Use-dependent facilitation and depression of L-type Ca2+ current in guinea-pig ventricular myocytes: modulation by Ca2+ and isoprenaline. Cardiovasc. Res. 44, 381-389.

Bers, D.M., 1983. Early transient depletion of extracellular Ca during individual cardiac muscle contractions. Am. J. Physiol. 244, H462-H468.

Bers, D.M., MacLeod, K.T., 1986. Cumulative depletions of extracellular calcium in rabbit ventricular muscle monitored with calcium-selective microelectrodes. Circ. Res. 58, 769-782.

Blatter, L.A., Niggli, E., 1998. Confocal near-membrane detection of calcium in cardiac myocytes. Cell Calcium 23, 269-279.

Brette, F., Leroy, J., Le Guennec, J.Y., Sallé, L., 2005a. Ca^{2+} currents in cardiac myocytes: Old story, new insights. Prog. Biophys. Mol. Biol. 91, 1-82.

Brette, F., Korchev, Y., Orchard, C. H., 2005b, Cardiac and neuronal sodium currents are differentially localized in rat ventricular myocytes: J Physiol, 567P, PC29 Abstract.

Brette, F., Orchard, C., 2003. T-tubule function in mammalian cardiac myocytes. Circ. Res. 92, 1182-1192.

Brette, F., Sallé, L., Orchard, C. H., 2005c, Role of t-tubules in calcium entry in rat ventricular myocytes: importance of I_{Ca}: Journal of Molecular and Cellular Cardiology, 39, 180 Abstract.

Brette, F., Sallé, L., Orchard, C.H., 2006. Quantification of calcium entry at the T-tubules and surface membrane in rat ventricular myocytes. Biophys. J. 90, 381-389.

Caillé, J., Ildefonse, M., Rougier, O., 1985. Excitation-contraction coupling in skeletal muscle. Prog. Biophys. Mol. Biol. 46, 185-239.

Christé, G., 1999. Localization of K^+ channels in the T-tubules of cardiomyocytes as suggested by the parallel decay of membrane capacitance, IK_1 and IK_{ATP} during culture and by delayed IK_1 response to barium. J. Mol. Cell. Cardiol. 31, 2207-2213.

Clark, R.B., Tremblay, A., Melnyk, P., Allen, B.G., Giles, W.R., Fiset, C., 2001. T-tubule localization of the inward rectifier K^+ channel in mouse ventricular myocytes: a role in K^+ accumulation. J. Physiol. 537.3, 979-992.

Cooklin, M., Wallis, W.R., Sheridan, D.J., Fry, C.H., 1998. Conduction velocity and gap junction resistance in hypertrophied, hypoxic guinea-pig left ventricular myocardium. Exp. Physiol. 83, 763-770.

Daut, J., 1982. The passive electrical properties of guinea-pig ventricular muscle as examined with a voltage-clamp technique. J. Physiol. 330, 221-242.

Egan, T.M., Noble, D., Noble, S.J., Powell, T., Spindler, A.J., Twist, V.W., 1989. Sodium-calcium exchange during the action potential in guinea-pig ventricular cells. J. Physiol. 411, 639-661.

Faber, G.M., Rudy, Y., 2000. Action potential and contractility changes in $[Na^+]_i$ overloaded cardiac myocytes. A simulation study. Biophys. J. 78, 2392-2404.

Findlay, I., 2002. Voltage-dependent inactivation of L-type Ca^{2+} currents in guinea-pig ventricular myocytes. J. Physiol. 545.2, 389-397.

Forbes, M.S., Hawkey, L.A., Sperelakis, N., 1984. The transverse-axial tubular system (TATS) of mouse myocardium: its morphology in the developing and adult animal. Am. J. Anat. 170, 143-162.

Forbes, M.S., Sperelakis, N., 1976. The presence of transverse and axial tubules in the ventricular myocardium of embryonic and neonatal guinea pigs. Cell Tissue Res. 166, 83-90.

Frank, J.S., Mottino, G., Reid, D., Molday, R.S., Philipson, K.D., 1992. Distribution of the Na^{+}-Ca^{2+} exchange protein in mammalian cardiac myocytes: an immunofluorescence and immunocolloidal gold-labeling study. J. Cell Biol. 117, 337-345.

Gao, J., Mathias, R.T., Cohen, I.S., Baldo, G.J., 1995. Two functionally different Na/K pumps in cardiac ventricular myocytes. J. Gen. Physiol. 106, 995-1030.

Grantham, C.J., Cannell, M.B., 1996. Ca^{2+} influx during the cardiac action potential in guinea pig ventricular myocytes. Circ. Res. 79, 194-200.

Hund, T.J., Kucera, J.P., Otani, N.F., Rudy, Y., 2001. Ionic charge conservation and long-term steady-state in the Luo-Rudy dynamic cell model. Biophys. J. 81, 3324-3331.

Hilgemann, D.W., Noble, D., 1987. Excitation-contraction coupling and extracellular calcium transients in rabbit atrium: reconstruction of basic cellular mechanisms. Proc. R. Soc. Lond. B230, 163-205.

Huxley, H.E., 1964. Evidence for continuity between the central elements of the triads and the extracellular space in frog *sartorius* muscle. Nature 202, 1067-1071.

Iwata, Y., Hanada, H., Takahashi, M., Shigekawa, M., 1994. Ca^{2+}-ATPase distributes differently in cardiac sarcolemma than dihydropyridine receptor alpha 1 subunit and Na^{+}/Ca^{2+} exchanger. FEBS Lett. 355, 65-68.

Jafri, M.S., Rice, J.J., Winslow, R.L., 1998. Cardiac Ca^{2+} dynamics: the roles of ryanodine receptor adaptation and sarcoplasmic reticulum load. Biophys. J. 74, 1149-1168.

Kieval, R.S., Bloch, R.J., Lindenmayer, G.E., Ambesi, A., Lederer, W.J., 1992. Immunofluorescence localization of the Na-Ca exchanger in heart cells. Am. J. Physiol. 263, C545-C550.

Korchev, Y.E., Negulyaev, Y.A., Edwards, C.R.W., Vodyanov, I., Lab, M.J., 2000. Functional localization of single active ion channels on the surface of a living cell. Nature Cell Biol. 2, 616-619.

Li, G.R., Lau, C.P., Shrier, A., 2002. Heterogeneity of sodium current in atrial vs epicardial ventricular myocytes of adult guinea pig hearts. J. Mol. Cell. Cardiol. 34, 1185-1194.

Lu, S., Holst, M. J., Bank, R. E., McCulloch, A. D., Michailova, A., 2005, 3D model of synchronous calcium signals in ventricular myocyte: Biophysical Journal, v. 2005 Biophys. Soc. p. 664-Pos Abstract.

McDonough, A.A., Zhang, Y., Shin, V., Frank, J.S., 1996. Subcellular distribution of sodium pump isoform subunits in mammalian cardiac myocytes. Am. J. Physiol. 270, C1221-C1227.

McGuigan, J.A.S., 1974. Some limitations of the double sucrose gap and its use in a study of the slow outward current in mammalian ventricular muscle. J. Physiol. 240, 775-806.

Nagatomo, T., Fan, Z., Ye, B., Tonkovich, G.S., January, C.T., Kyle, J.W., Makielski, J.C., 1998. Temperature dependence of early and late currents in human cardiac wild-type and long Q-T DeltaKPQ Na+ channels. Am. J. Physiol. 275, H2016-H2024.

Noble, D., Varghese, A., Kohl, P., Noble, P., 1998. Improved guinea-pig ventricular cell model incorporating a diadic space, IK_r and IK_s, and length- and tension-dependent processes. Can. J. Cardiol. 14, 123-134.

Noble, D., 2002. Modeling the heart--from genes to cells to the whole organ. Science 295, 1678-1682.

Nordin, C., 1993. Computer model of membrane current and intracellular Ca^{2+} flux in the isolated guinea pig ventricular myocyte. Am. J. Physiol. 265, H2117-H2136.

Nordin, C., Ming, Z., 1995. Computer model of current-induced early afterdepolarizations in guinea pig ventricular myocytes. Am. J. Physiol. 268, H2440-H2459.

Page, E., McAllister, L.P., 1973. Quantitative electron microscopic description of heart muscle cells: application to normal, hypertrophied and thyroxin treated hearts. Am. J. Cardiol. 31, 172-181.

Pager, J., 1971. Etude morphométrique du système tubulaire transverse du myocarde ventriculaire de rat. J. Cell Biol. 50, 233-237.

Pasek, M., Christé, G., Simurda, J., 2003. A quantitative model of cardiac ventricular cell incorporating the transverse-axial tubular system. Gen. Physiol. Biophys. 22, 355-368.

Pasek, M., Simurda, J., Christé, G., 2006. The functional role of cardiac T-tubules explored in a model of rat ventricular myocytes. Philos. Transact. A Math. Phys. Eng. Sci. 364, 1187-1206.

Pasek, M., Simurda, J., Christé, G., Orchard, C., 2007. Modelling the cardiac transverse-axial tubular system. Prog. Biophys. Mol. Biol. Present issue.

Puglisi, J.L., Wang, F., Bers, D.M., 2004. Modeling the isolated cardiac myocyte. Prog. Biophys. Mol. Biol. 85, 163-178.

Rasmussen, H.B., Moller, M., Knaus, H.G., Jensen, B.S., Olesen, S.P., Jorgensen, N.K., 2004. Subcellular localization of the delayed rectifier potassium channels KCNQ1 and ERG1 in the rat heart. Am. J. Physiol. 286, H11300-H1309.

Sakmann, B.F., Spindler, A.J., Bryant, S.M., Linz, K.W., Noble, D., 2000. Distribution of a persistent sodium current across the ventricular wall in guinea pigs. Circ. Res. 87, 910-914.

Scriven, D.R., Dan, P., Moore, E.D., 2000. Distribution of proteins implicated in excitation-contraction coupling in rat ventricular myocytes. Biophys. J. 79, 2682-2691.

Shepherd, N., McDonough, H.B., 1998. Ionic diffusion in transverse tubules of cardiac ventricular myocytes. Am. J. Physiol. 275, H852-H860.

Simurda, J., Pasek, M., Christé, G., Simurdova, M., 2004. Modelling the distribution of [Ca^{2+}] within the cardiac T-tubule - Effects of Ca^{2+} current distribution and changes in extracellular [Ca^{2+}]. J. Physiol. 561P, 13P Abstract.

Siri, F.M., Krueger, J., Nordin, C., Ming, Z., Aronson, R.S., 1991. Depressed intracellular calcium transients and contraction in myocytes from hypertrophied and failing guinea pig hearts. Am. J. Physiol. 261, H514-H530.

Soeller, C., Cannell, M.B., 1999. Examination of the transverse tubular system in living cardiac rat myocytes by 2-photon microscopy and digital image-processing techniques. Circ. Res. 84, 266-275.

Taniguchi, A., Toyama, J., Kodama, I., Anno, T., Shirakawa, M., Usui, S., 1994. Inhomogeneity of cellular activation time and V_{max} in normal myocardial tissue under electrical field stimulation. Am. J. Physiol. 267, H694-H705.

Thomas, M.J., Sjaastad, I., Andersen, K., Helm, P.J., Wasserstrom, J.A., Sejersted, O.M., Ottersen, O.P., 2003. Localization and function of the Na+/Ca2+ exchanger in normal and detubulated rat cardiomyocytes. J. Mol. Cell. Cardiol. 35, 1325-1337.

Tourneur, Y., Marion, A., Gautier, P., 1994. SR47063, a potent channel opener, activates K_{ATP} and a time-dependent current likely due to potassium accumulation. J. Membr. Biol. 142, 337-347.

Wang, D.Y., Chae, S.W., Gong, Q.Y., Lee, C.O., 1988. Role of a_{iNa} in positive force-frequency staircase in guinea pig papillary muscle. Am. J. Physiol. 255, C798-C807.

Wang, Z., Mitsuiye, T., Rees, S.A., Noma, A., 1997. Regulatory volume decrease of cardiac myocytes induced by □-adrenergic activation of the Cl^- channel in guinea pig. J. Gen. Physiol. 110, 73-82.

Yang, Z., Pascarel, C., Steele, D.S., Komukai, K., Brette, F., Orchard, C.H., 2002. Na+-Ca2+ exchange activity is localized in the T-tubules of rat ventricular myocytes. Circ. Res. 91, 315-322.

Yasui, K., Anno, T., Kamiya, K., Boyett, M.R., Kodama, I., Toyama, J., 1993. Contribution of potassium accumulation in narrow extracellular spaces to the genesis of nicorandil-induced large inward tail current in guinea-pig ventricular cells. Pflügers Arch. 422, 371-379.

Zeng, J., Laurita, K.R., Rosenbaum, D.S., Rudy, Y., Laurita, K., Rosenbaum, D., 1995. Two components of the delayed rectifier K^+ current in ventricular myocytes of the guinea pig type. Theoretical formulation and their role in repolarization. Circ. Res. 77, 140-152.

Legends to tables

Table 1. Electrical properties of surface and tubular membrane ion transport systems used in the model. First column: parameters of individual transporters (maximum conductivities (g), permeabilities (P) or currents (I_{max})). Second column: values of parameters related to total membrane. Third and fourth columns: values related to surface and tubular membrane respectively. All values in the table are expressed per unit area of membrane (specified in fourth panel). In model equations as used for simulations (see Appendix 1 as online supplementary material) the values are recomputed to the whole cell by multiplying by corresponding membrane area (S_{ms} = 5.065 $\times 10^{-5}$ cm^2 and S_{mt} = 5.6225 $\times 10^{-5}$ cm^2). The last column shows the fractions of ion transporters in the tubular membrane (see text for further details). When no data could be found, the densities of ionic transfer mechanisms were assumed to be equally distributed between both membrane systems.

Table 2. Action potential duration at 90% repolarisation (APD_{90}), peak $[Ca^{2+}]_i$ ($[Ca^{2+}]_{i,peak}$), end-diastolic $[Ca^{2+}]_i$ ($[Ca^{2+}]_{i,end}$), $[Na^+]_i$ ($[Na^+]_{i,end}$) and $[K^+]_i$ ($[K^+]_{i,end}$) during steady state stimulation at the frequencies indicated. For 0 Hz, the values correspond to the
990 first action potential after resting steady-state.

Table 3. Ca^{2+} and K^{+} concentration changes in TATS during simulation of a steady-state cycle at 1 Hz, 4 Hz and 6 Hz. Reference values are the extracellular ion concentrations. A) Results from the basic model. B) Results from the model with slower rate of Ca^{2+} diffusion ($\tau_{Ca,t}$ = 1.3 s) between tubular and extracellular space.

Table 4. Relative changes in the amount of charge transferred by $I_{CaL,t}$ ($\Delta Q_{Ca,t}$), $I_{NaCa,t}$ ($\Delta Q_{NaCa,t}$), and $I_{K1,t}$ ($\Delta Q_{K1,t}$), compared with when ion concentrations within the TATS were fixed at bulk extracellular levels. The amount of charge transferred during one second from the onset of the pulse or of the AP applied from rest, was computed from data shown in Fig. 10.

Table 5. Relative changes in the amount of charge transferred by $I_{CaL,t}$ ($\Delta Q_{Ca,t}$), $I_{NaCa,t}$ ($\Delta Q_{NaCa,t}$), $I_{Ks,t}$ + $I_{Kr,t}$ ($\Delta Q_{K,t}$) and $I_{K1,t}$ ($\Delta Q_{K1,t}$) during one cycle at steady-state, as compared with when ion concentrations in TATS were fixed at extracellular levels: A) in the basic model, B) in the model with slower rate of Ca^{2+} diffusion ($\tau_{Ca,t}$ = 1.3 s) between tubular and extracellular space.

Figure legends:

Figure 1. A: Schematic diagram of the ventricular cell model. The description of electrical activity of the surface (s) and tubular (t) membranes comprises formulation of the ion transporters shown. The intracellular space contains the subspace, the Ca^{2+}-network (NSR) and junctional (JSR) compartments of sarcoplasmic reticulum and the Ca^{2+} buffers calmodulin (B_{cm}), troponin (B_{htrpn}, B_{ltrpn}) and calsequestrin (B_{cs}). The small filled rectangles in JSR membrane represent ryanodine receptors. The small bi-directional arrows denote Ca^{2+} diffusion. Ion diffusion between the tubular and the extracellular space is represented by the dashed arrow. **B.** Electrical interaction between the surface and tubular membrane. V_{ms}, I_{ms}, I_{is}, I_{Cs}, C_s and V_{mt}, I_{mt}, I_{it},, I_{Ct}, C_t are, respectively, membrane voltage, total membrane current, total ionic current, capacitance current and membrane capacity of the surface and tubular membranes. R_{st} is the mean lumenal resistance of the TATS and R_{el} series resistance of microelectrode.

Figure 2. Model reconstruction of experiments published by Shepherd and McDonough (1998). The squares show model output, the solid line shows the bi-exponential function fitted by these authors to experimental data. **A:** Analysis of the rate of Na^+ diffusion between extracellular and tubular space. The traces show the time course of normalized ΔI_{Na} obtained at various times after a rapid change of bath $[Na^+]$ from 150 to 105 mM. **Inset**: same data, detailed view of early change. **B:** Analysis of the rate of Ca^{2+} diffusion between extracellular and tubular space. The traces show the time course of normalized ΔI_{CaL} obtained at various times after a rapid change of bath $[Ca^{2+}]$ from 0.45 to 1.8 mM. **Inset**: same data, detailed view of early change.

Figure 3. Stability of the model with time. The model was run from stabilised values obtained from the resting steady state after 6 hours virtual cell life (not shown). The model was used to simulate: (i) 3 hours at rest in 5.4 mM extracellular $[K^+]$ ($[K^+]_e$), followed by 1 hour regular stimulation at a frequency (F_s) of 4 Hz.; (ii) a new period of 3 hours at rest followed by a one minute exposure to 0.5 mM $[K^+]_e$, followed by a final period of 3 hours at rest. In the figure, for clarity, samples of 5 or 10 minutes duration were taken at times indicated on the horizontal axis to show transient changes and stabilised values. During the period of stimulation at 4 Hz, the model was designed to output the values of variables at the end of each diastolic interval. The top two rows show the changes of stimulation frequency (F_s) and extracellular K^+ concentration ($[K^+]_e$) imposed on the model.

Figure 4. Model action potentials compared with those from GP cells. Action potentials from the model (right) were generated at stimulation frequencies of 1, 2, 3, 4, and 5 Hz to compare with the experimental data in figure 1 of Wang et al. (1988). Their action potential data at the same frequencies were extracted and digitised and are shown in the left panel. Note the similar rate-dependent shortening of action potential duration and decrease of action potential amplitude.

1050 **Figure 5.** Action potentials, intracellular [Ca^{2+}], I_{CaL}, I_{NaCa} and I_{NaK} produced by the model when stimulated from steady-state resting conditions (1st beat, 0 Hz) and during steady-state stimulation at 2, 4 and 6 Hz. Traces referring to surface membrane are solid lines, those referring to tubular membrane are dotted lines. APs in both regions are practically identical.

Figure 6. Analytical solution of the time course of capacitance current in the model. **A**: simplified equivalent electrical circuit of the cell with linearised current-voltage relation around the resting voltage. The values R_{ms} = 67 MΩ and R_{mt} = 18 MΩ are minimum chord resistances of the surface and tubular membranes estimated from the complete model in the voltage range -85 ±10 mV. **B**: analytical solution of the time course of membrane current I_m in response to 10 mV hyperpolarizing impulse ($I_m = I_1\, exp(-t/\tau_1) + I_2\, exp(-t/\tau_2) + I_o$; τ_1= 52.6 μs, τ_2 = 0.92 μs). Time courses of individual components of resolved I_m (calculated at R_{el} = 0.5 MΩ, R_{st} = 35.18 kΩ) are labelled by numbers. The total I_m -trace only minutely differs from its single exponential component $I_1\, exp(-t/\tau_1)$ (labelled 1), and relaxes towards the steady state value I_o (trace labelled 0). Inset: the negligible fast component $I_2\, exp(-t/\tau_2)$ (labelled 2) is shown enlarged. **C**: analytical solution of time course of membrane voltages V_{ms} and V_{mt} at surface and tubular membranes expressed as a sum of exponential components with time constants $\tau_1$and τ_2 identical to those of I_m. The faster component appears to be negligible and both traces are nearly identical. **Inset to C**: initial part of the responses in an expanded scaling showing the initial time course of the difference V_{ms}-V_{mt}. **D**: Numerical simulation of I_m, V_{ms} and V_{mt} obtained from the complete model with TATS. A 10 mV pulse was applied at rested state when held at the zero current voltage of -85.53 mV (plotted as 0 mV). The current computed by the model is represented by symbols connected with a dotted line. Superimposed with the charging current continuous lines represent the fit by either a single exponential function or a double exponential function. Thus panel D represents one set of model output data and two fitting curves superimposed. The model output data and fitting curves can hardly be distinguished from each other. Neither can they be distinguished from the analytical solution of the simplified linearised model (B and C). **E**: The time courses of V_{ms} and V_{mt} (see expanded view of initial time course in inset) are almost identical to the theoretical ones in panel C.

Figure 7. Voltage homogeneity in voltage clamp and in current clamp (A) Response of the model cell to a 75 mV depolarising pulse with R_{el} = 0.5 MΩ. Upper panel: imposed voltage step (V_c). Middle panel: superimposed voltages across the surface (V_{ms}) and tubular (V_{mt}) membranes and the command voltage (the thick black line is V_{ms}, V_{mt} is the gray line superimposed onto the middle of the thick black line and the thin black line is the rectangular command pulse V_c); local maxima in V_{ms} and V_{mt} appear at peak I_{Na} (a) and at peak I_{CaL} (b). Lower panel: difference V_{ms} - V_{mt}. (B) Upper panel: imposed current stimulus. Middle panel: superimposed action potentials at the surface (V_{ms} thick black line) and tubular (V_{mt} superimposed gray line) membranes generated by the model during steady state stimulation at 4 Hz. Lower panel: the difference V_{ms} - V_{mt} at enlarged scale. Apart from an initial positive surge due to the stimulating pulse, the difference peaks at -188 μV during fast depolarisation phase and is less than ± 3 μV throughout repolarisation phases.

Figure 8. Intrinsic action potentials of the tubular and surface membranes. Action potentials were computed during 4 Hz steady-state stimulation. At the end of the stimulating pulse (4.8 nA, 1ms), the membrane systems were disconnected and individual APs were recorded (full traces). The differences became negligible if tight electrical coupling between both systems was maintained (dashed trace).

Figure 9. Changes of tubular ionic concentrations during cellular activity. Tubular concentrations $[Ca^{2+}]_t$ (A and D), $[K^+]_t$ (B and E) and $[Na^+]_t$ (C and F) were recorded at steady-state in current clamp mode using the basic model. Panels A, B and C show the time course of tubular concentrations during one cycle at 4 Hz. The steady state values attained at rest and the values of extracellular ion concentrations are also plotted. The stimulating pulse was delivered at time zero. Panels D, E and F show the maximum and minimum tubular concentrations during one cycle at stimulation frequencies from 1 to 6 Hz. The values are expressed as percentage changes from the corresponding extracellular concentrations: 1.8 mM for $[Ca^{2+}]_e$, 5.4 mM for $[K^+]_e$ and 140 mM for $[Na^+]_e$. Note the different scales on panel D-F.

Figure 10. Effect of changes of tubular ion concentrations on tubular ionic currents $I_{CaL,t}$, $I_{NaCa,,t}$ and $I_{K1,t}$. A) Response to 0.2 s voltage clamp impulse from resting voltage (-85.54 mV) to 20 mV. B) Response during AP elicited from resting voltage by current clamp. Dotted lines: basic unmodified model with variable tubular ionic concentrations, solid lines: modified model with tubular concentration fixed at bulk extracellular levels.

Figure 11. Effect of changes of tubular ion concentrations on Ca^{2+} load in NSR ($[Ca^{2+}]_{NSR}$) and on the systolic Ca^{2+} transient. The model cell was stimulated at 1 Hz (A), 4 Hz (B) and 6 Hz (C) (steady-state). The solid line shows results from the model when ion concentrations in
1120 the TATS were fixed at extracellular levels. The dashed and dotted lines represent results from the basic model and from the model with increased time constant of ion exchange between tubular lumen and extracellular space (from 0.24 s to 1.3 s, respectively).

Figure 12. Effect of tubular ion concentrations on Ca^{2+} load in NSR ($[Ca^{2+}]_{NSR}$) after resuming stimulation (at 1 Hz) from resting steady-state. Solid, dashed and dotted lines: results from models described in the legend to Fig. 11. The effect of variable concentrations in TATS is negligible at rest but becomes significant during steady-state stimulation.

parameter	total membrane	surface membrane	tubular membrane	unit	fraction in TATS
g_{Na}	30	29.753	30.222	(mS cm^{-2})	0.57
g_{Naps}	0.0053	0.0053	0.0053	(mS cm^{-2})	0.526
g_{Kr}	0.0209	0.0209	0.0209	(mS cm^{-2})	0.526
g_{Ks}	0.1975	0.1975	0.1975	(mS cm^{-2})	0.526
g_{K1}	0.75	0.3165	1.1405	(mS/cm^{-2})	0.8
g_{Kp}	0.006	0.006	0.006	(mS cm^{-2})	0.526
$g_{K(Na)}$	0.1285	0.1285	0.1285	(mS cm^{-2})	0.526
$g_{K(ATP)}$	1	1	1	(mS cm^{-2})	0.526
$g_{Na,b}$	0.0007	0.0007	0.0007	(mS/cm^{-2})	0.526
$g_{Ca,b}$	0.0021	0.0021	0.0021	(mS/cm^{-2})	0.526
$P_{Ca,L}$	0.0048	0.0036	0.0058	(cm s^{-1})	0.64
$P_{K,L}$	4.80E-6	3.65E-6	5.84E-6	(cm s^{-1})	0.64
$P_{ns(Na)}$	1.75E-7	1.75E-7	1.75E-7	(cm s^{-1})	0.526
$P_{ns(Ca)}$	1.75E-7	1.75E-7	1.75E-7	(cm s^{-1})	0.526
$I_{pCa,max}$	1.15	1.9413	0.4372	(μA cm^{-2})	0.2
$I_{NaK,max}$	1.5	1.5	1.5	(μA cm^{-2})	0.526
k_{NaCa}	0.00025	0.00025	0.00025	(μA cm^{-2} mM^{-4})	0.526

Table 1. Electrical properties of surface and tubular ionic pathways used in the model.

Frequency	0 Hz	1 Hz	2 Hz	3 Hz	4 Hz	5 Hz	6 Hz
APD_{90} (ms)	188.2	159.7	137.8	121.7	109.2	99.8	93.1
$[Ca^{2+}]_{i,peak}$ (nM)	211	802	1157	1258	1237	1179	1114
$[Ca^{2+}]_{i,end}$ (nM)	37.4	88.8	138.5	176.2	204.5	230.1	255.6
$[Na^{+}]_{i,end}$ (mM)	8.1	11.1	12.2	12.7	13.1	13.4	13.6
$[K^{+}]_{i,end}$ (mM)	140.0	136.8	135.5	134.7	134.3	134.0	133.3

Table 2. AP durations and intracellular concentrations at steady state in the model run at various frequencies.

A

	1 Hz		4 Hz		6 Hz	
$\Delta[Ca^{2+}]_{t,rel}$ (%)	2.6	-13.8	0.9	-8.1	-0.9	-7.1

B

	1 Hz		4 Hz		6 Hz	
$\Delta[Ca^{2+}]_{t,rel}$ (%)	-0.4	-19.6	-10.6	-19.4	-14	-19.8

Table 3. Evaluation of the extent of Ca^{2+} concentration changes in TATS during a simulation of steady state cycle at 1 Hz, 4 Hz and 6 Hz.

	VC from rest	AP from rest
$\Delta Q_{CaL,t}$ (%)	-15.3	-8
$\Delta Q_{NaCa,t}$ (%)	0.9	1.1
$\Delta Q_{K1,t}$ (%)	-27	-9.6

Table 4. The effect of ion concentration changes in TATS on the charge transferred by tubular currents in voltage- and current-clamp conditions.

A

	1 Hz	4 Hz	6 Hz
$\Delta Q_{CaL,t}$ (%)	-5.8	-3.8	-4.2
$\Delta Q_{NaCa,t}$ (%)	1.4	5.8	9.1
$\Delta Q_{K,t}$ (%)	-3.8	-1.9	-2.1
$\Delta Q_{K1,t}$ (%)	-5.4	-5.4	-4.4

B

	1 Hz	4 Hz	6 Hz
$\Delta Q_{CaL,t}$ (%)	-8.7	-13.2	-15.4
$\Delta Q_{NaCa,t}$ (%)	7.4	28.9	44.7
$\Delta Q_{K,t}$ (%)	-5.1	-4.7	-4.9
$\Delta Q_{K1,t}$ (%)	-4.2	-3	-1.9

Table 5. Evaluation of the effect of ion concentration changes in TATS on the charge transferred by tubular currents in one cycle in the basic model (A) and in the model with slower Ca^{2+} diffusion between tubular and extracellular space (B).

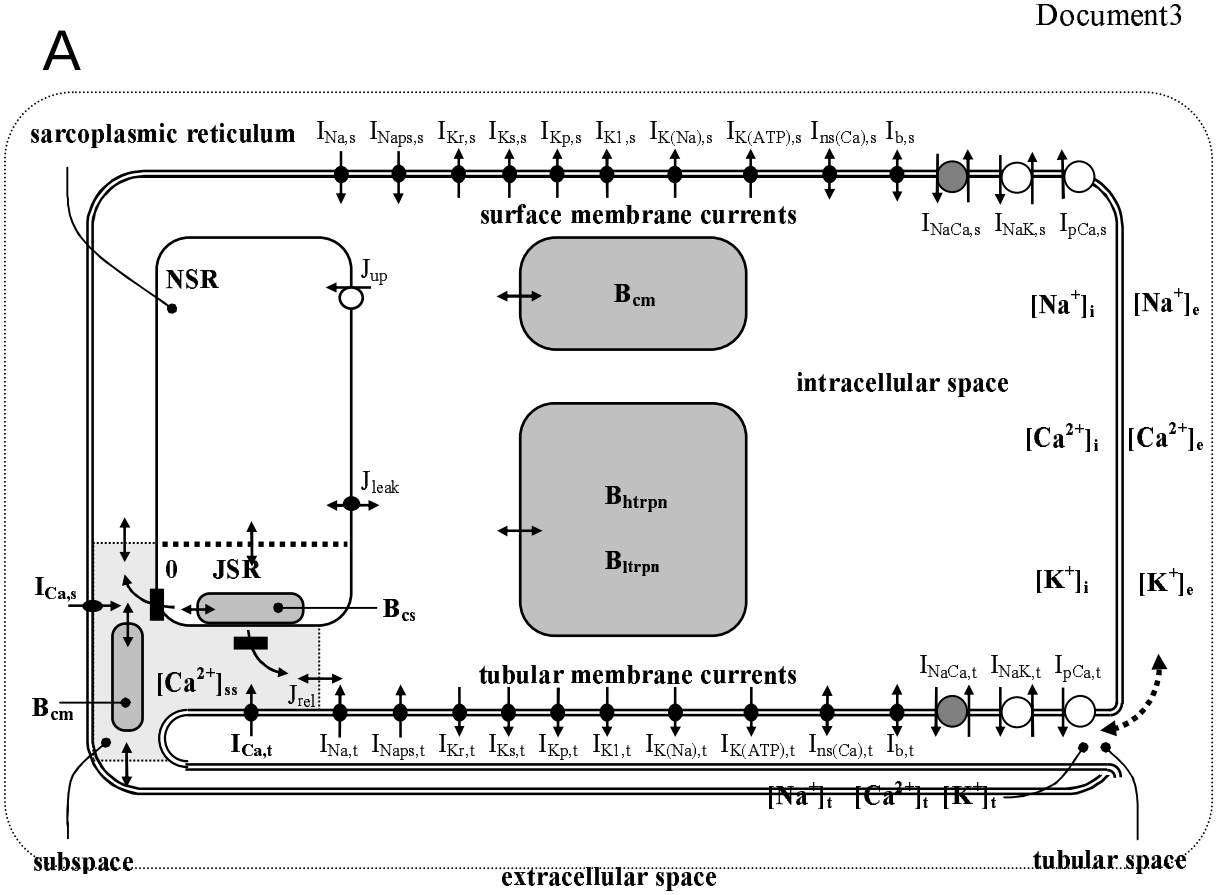

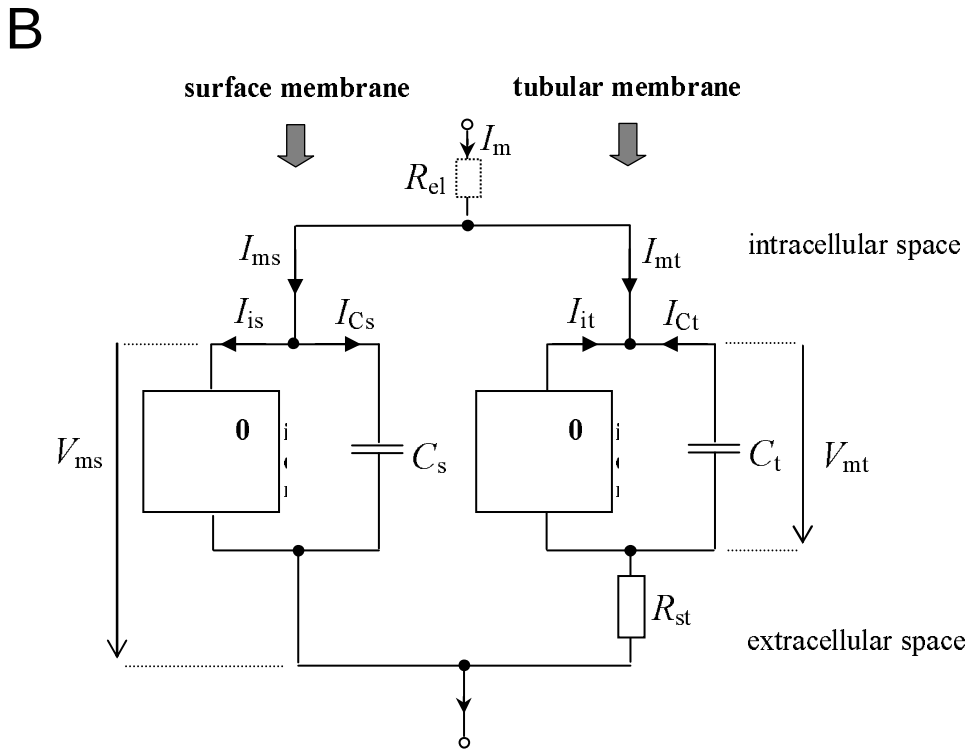

Figure 1. A: Schematic diagram of the ventricular cell model. B: Electrical equivalent scheme of the cellular membrane systems.

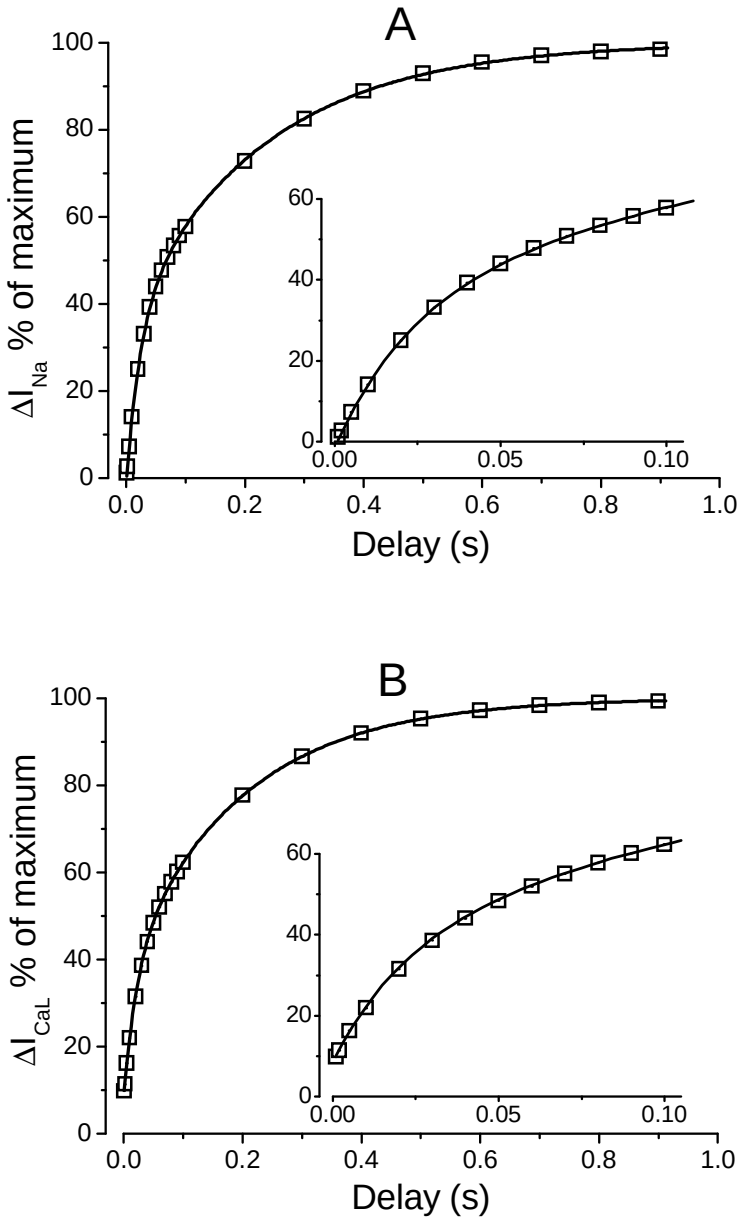

Figure 2. Model reconstruction of Na^+ diffusion (A) and Ca^{2+} diffusion (B) experiments of Shepherd and McDonough (1998).

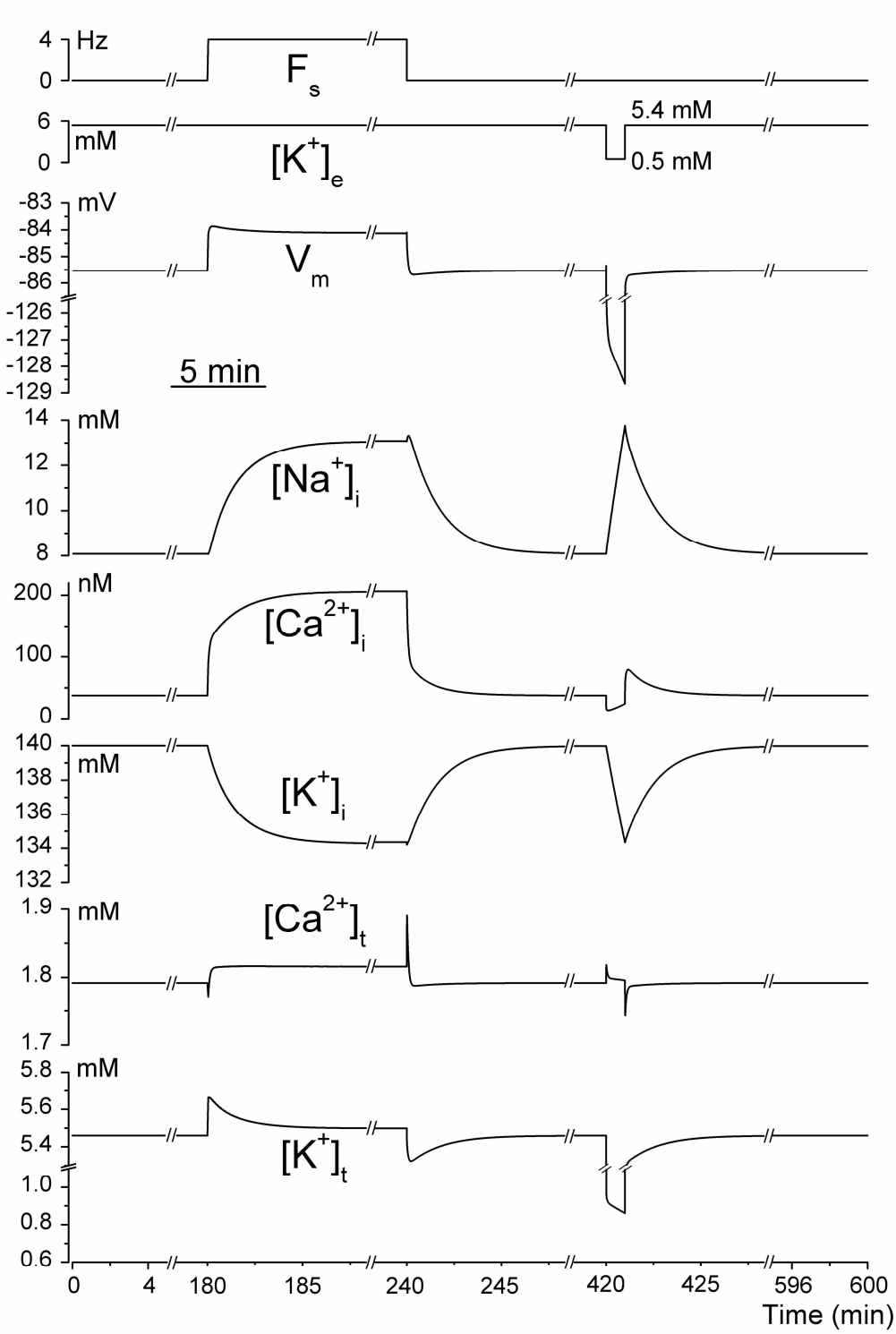

Figure 3. Test of stability of the model along time.

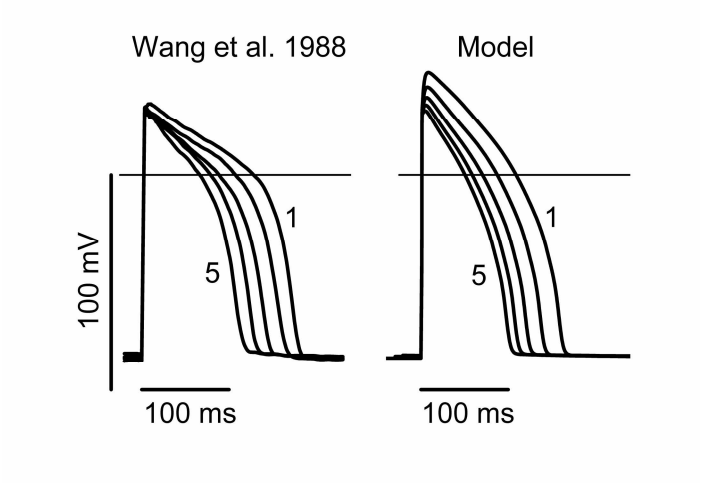

Figure 4. Action potentials in the model as compared with those from guinea-pig cells.

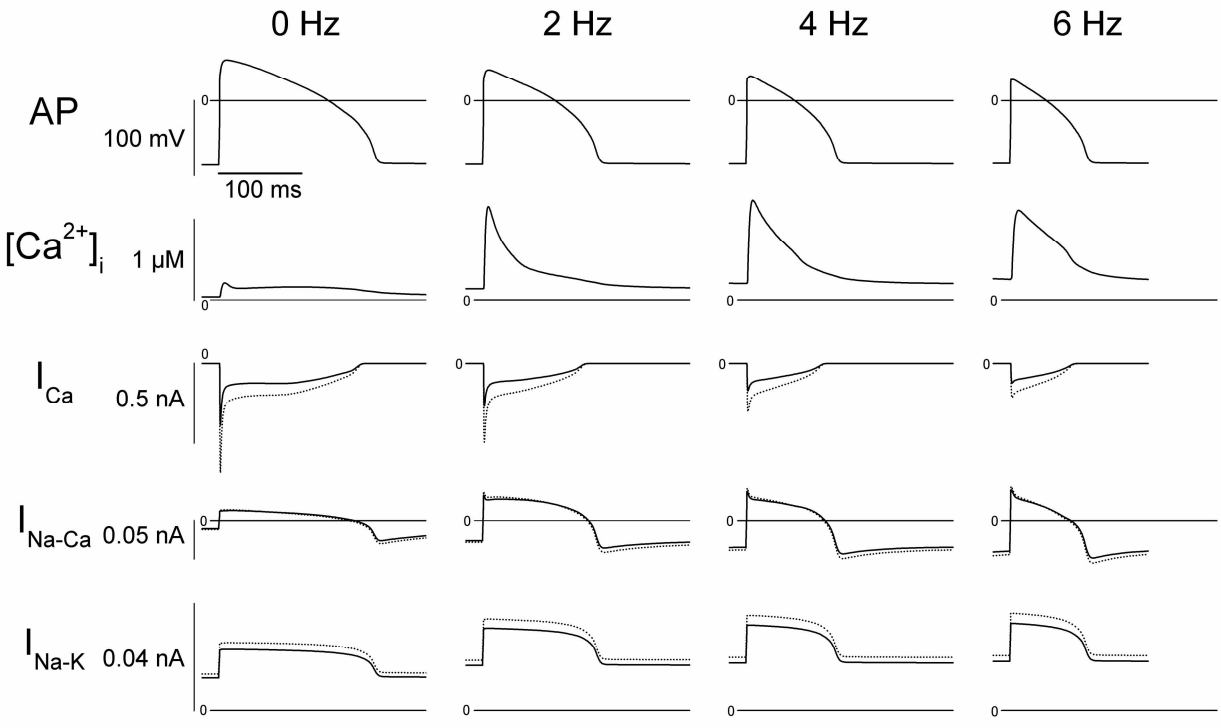

Figure 5. Action potentials, $[Ca^{2+}]_i$ and currents at surface and TATS in the model cell.

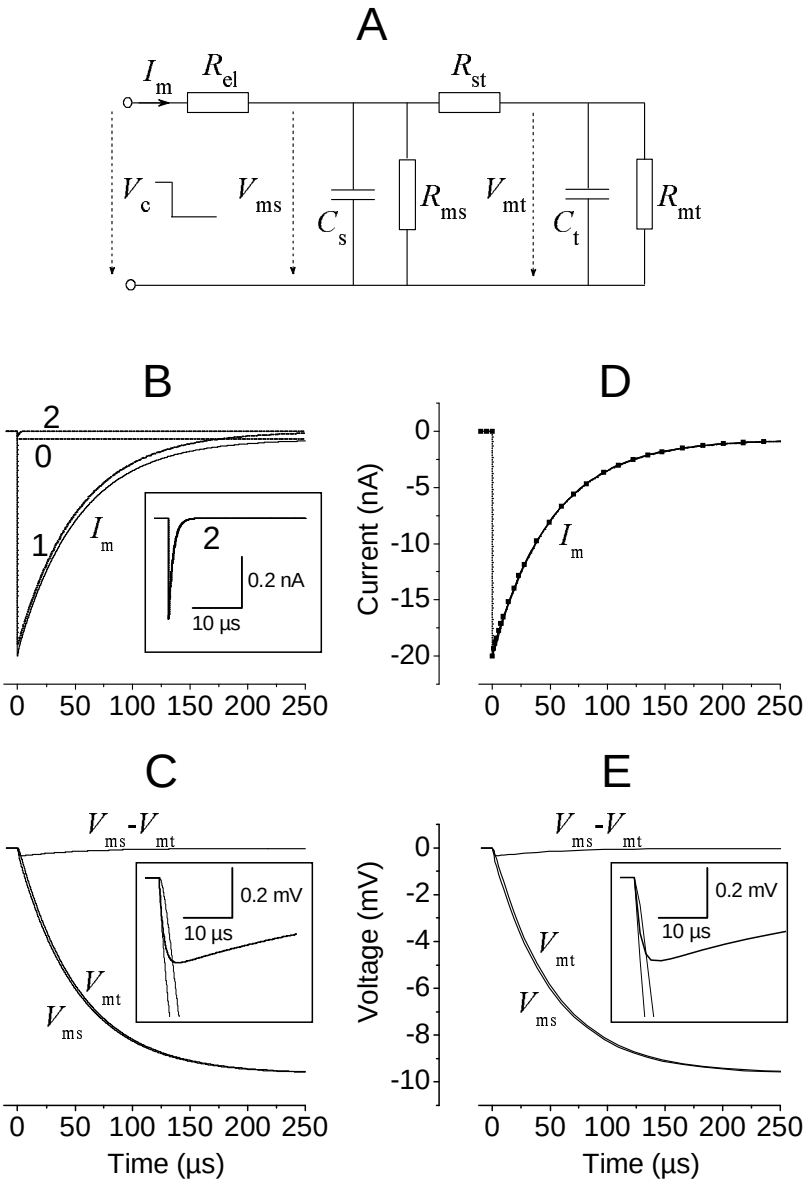

Figure 6. Passive properties of the cell with TATS.

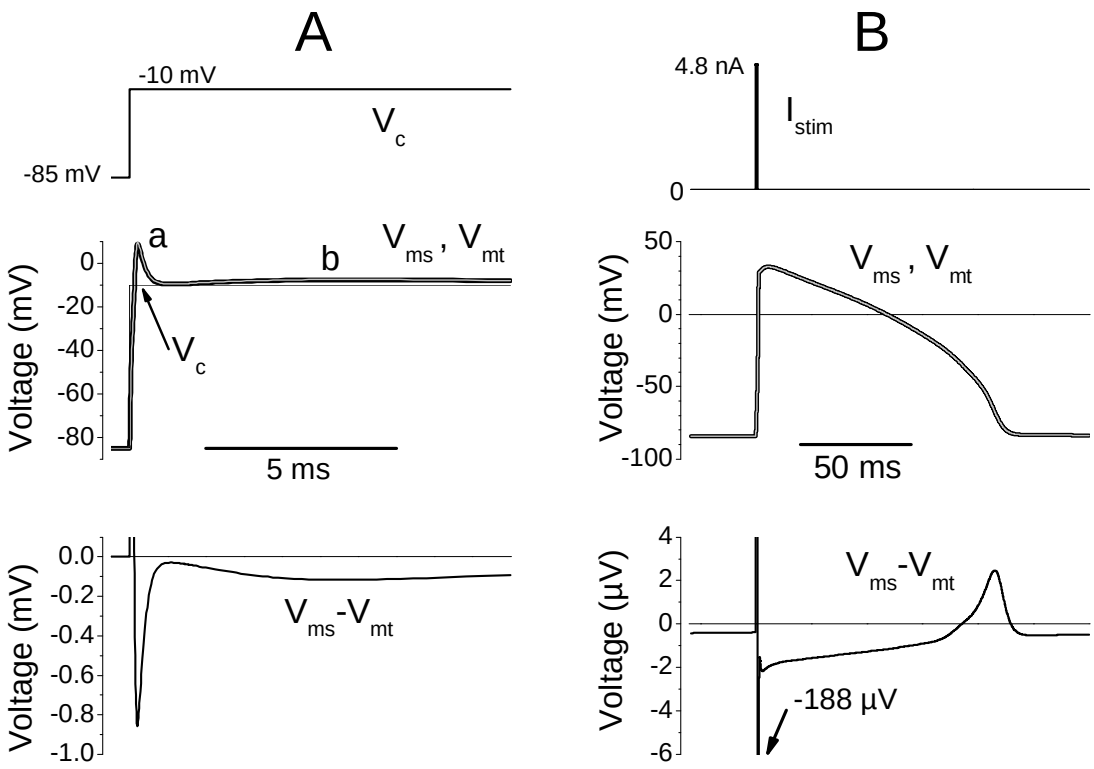

Figure 7. Voltage homogeneity in voltage-clamp and in current-clamp.

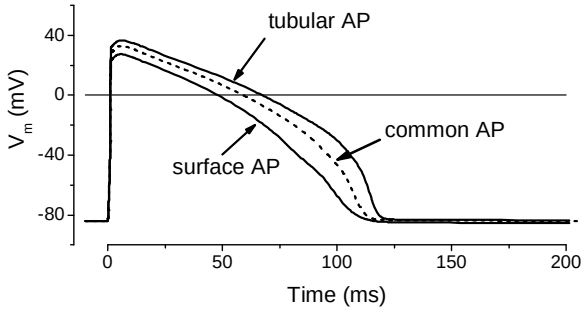

Figure 8. Electrical coupling dissipates differences between action potentials generated by isolated tubular and surface membranes.

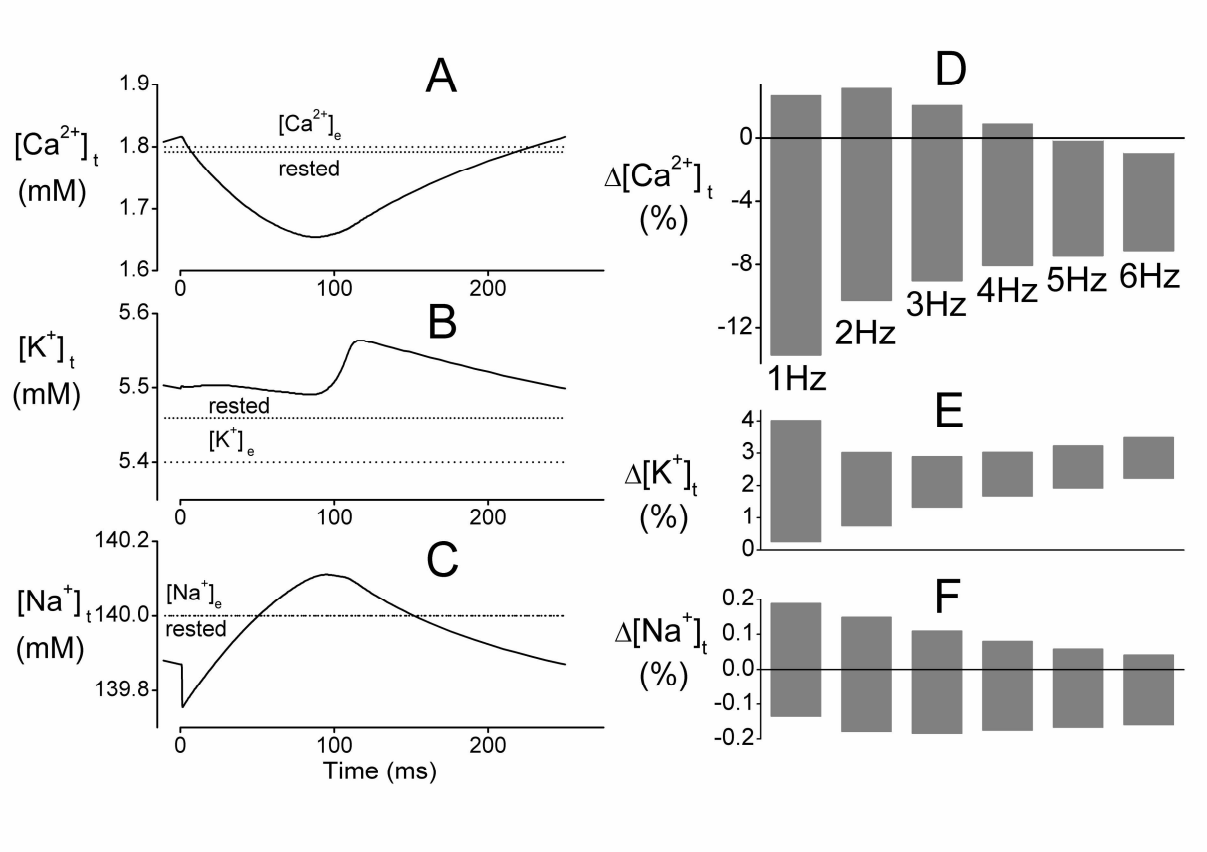

Figure 9. Changes of tubular ionic concentrations during cellular activity.

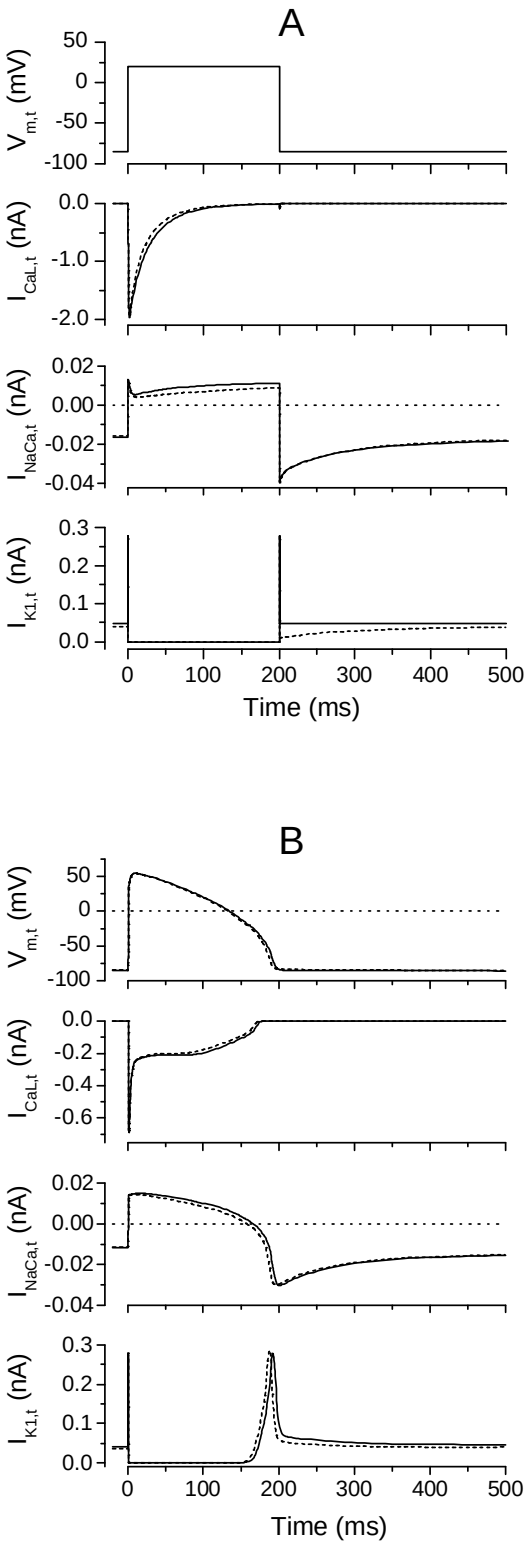

Figure 10. Evaluation of the effects of changes of tubular ionic concentrations on ionic currents.

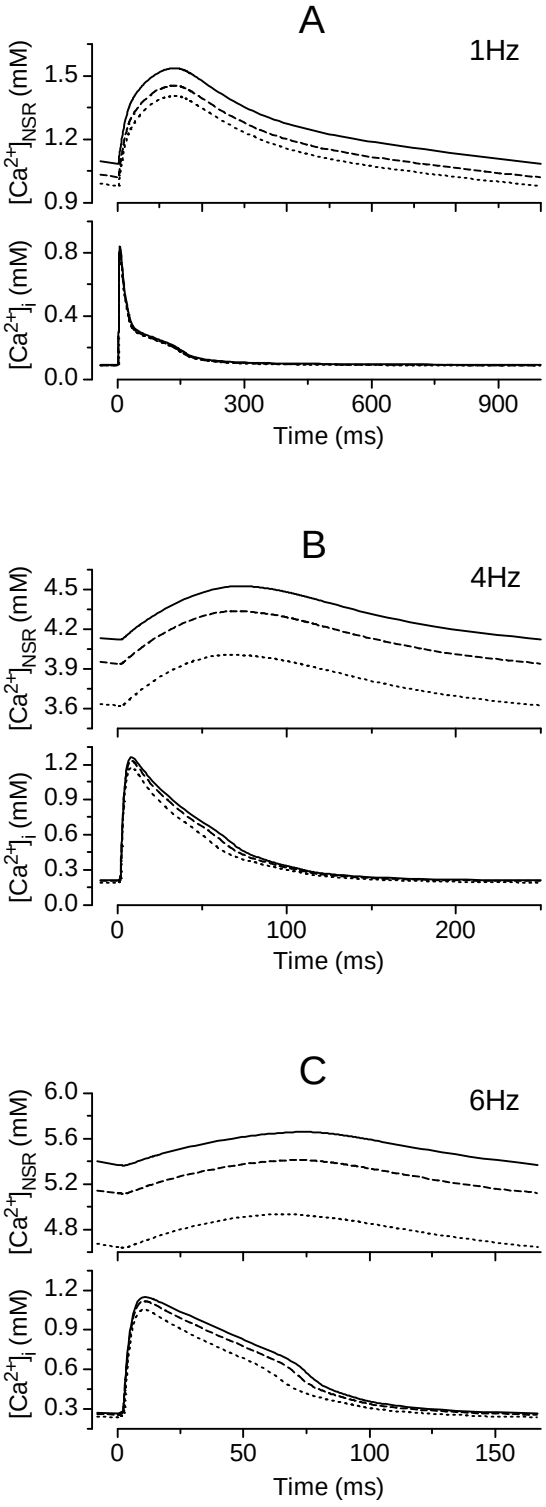

Figure 11. Effect of changes of tubular ion concentrations on Ca^{2+} load in NSR and on intracellular Ca^{2+} transients in physiological conditions.

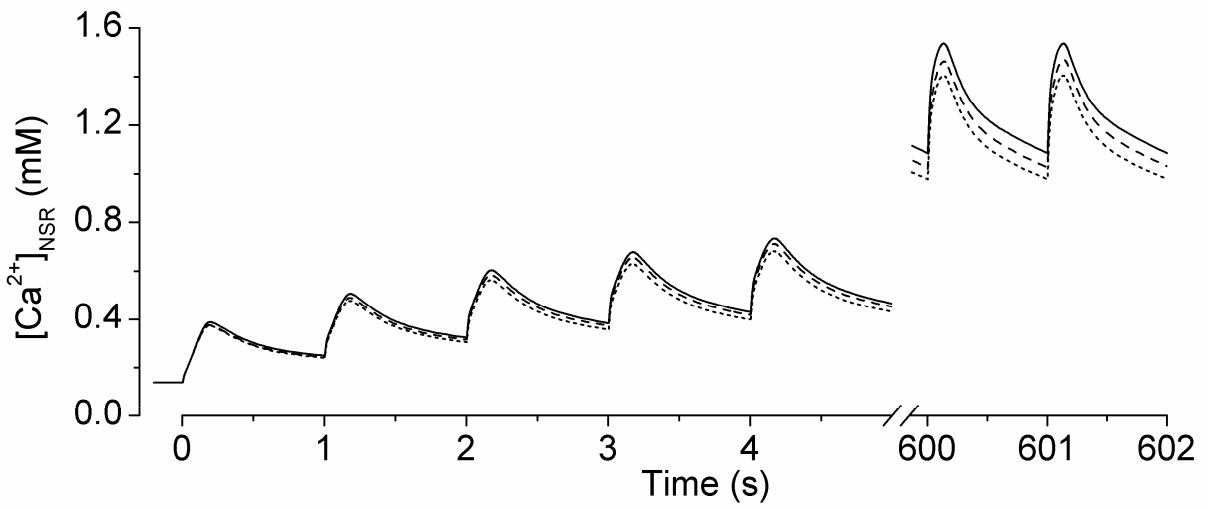

Figure 12. Effect of changes of tubular ion concentrations on Ca^{2+} load in NSR ($[Ca^{2+}]_{NSR}$) during 1 Hz stimulation from resting steady state.